

## Article

# Using a Neural Network to Model the Incidence Angle Dependency of Backscatter to Produce Seamless, Analysis-Ready Backscatter Composites over Land

Claudio Navacchi , Felix Reuß  and Wolfgang Wagner 

Department of Geodesy and Geoinformation, TU Wien, 1040 Vienna, Austria; felix.reuss@geo.tuwien.ac.at (F.R.); wolfgang.wagner@geo.tuwien.ac.at (W.W.)

\* Correspondence: claudio.navacchi@geo.tuwien.ac.at

**Abstract:** In order to improve the current standard of analysis-ready Synthetic Aperture Radar (SAR) backscatter data, we introduce a machine learning-based approach to estimate the slope of the backscatter–incidence angle relationship from several backscatter statistics. The method requires information from radiometric terrain-corrected gamma nought time series and overcomes the constraints of a limited orbital coverage, as exemplified with the Sentinel-1 constellation. The derived slope estimates contain valuable information on scattering characteristics of different land cover types, allowing for the correction of strong forward-scattering effects over water bodies and wetlands, as well as moderate surface scattering effects over bare soil and sparsely vegetated areas. Comparison of the estimated and computed slope values in areas with adequate orbital coverage shows good overall agreement, with an average RMSE value of 0.1 dB/° and an MAE of 0.05 dB/°. The discrepancy between RMSE and MAE indicates the presence of outliers in the computed slope, which are attributed to speckle and backscatter fluctuations over time. In contrast, the estimated slope excels with a smooth spatial appearance. After correcting backscatter values by normalising them to a certain reference incidence angle, orbital artefacts are significantly reduced. This becomes evident with differences up to 5 dB when aggregating the normalised backscatter measurements over certain time periods to create spatially seamless radar backscatter composites. Without being impacted by systematic differences in the illumination and physical properties of the terrain, these composites constitute a valuable foundation for land cover and land use mapping, as well as bio-geophysical parameter retrieval.

**Keywords:** Sentinel-1; radiometric terrain correction; analysis-ready data; incidence angle



Academic Editor: Massimiliano Pieraccini

Received: 27 October 2024

Revised: 26 December 2024

Accepted: 16 January 2025

Published: 22 January 2025

**Citation:** Navacchi, C.; Reuß, F.; Wagner, W. Using a Neural Network to Model the Incidence Angle Dependency of Backscatter to Produce Seamless, Analysis-Ready Backscatter Composites over Land. *Remote Sens.* **2025**, *17*, 361. <https://doi.org/10.3390/rs17030361>

**Copyright:** © 2025 by the authors. Licensee MDPI, Basel, Switzerland. This article is an open access article distributed under the terms and conditions of the Creative Commons Attribution (CC BY) license (<https://creativecommons.org/licenses/by/4.0/>).

## 1. Introduction

The last two decades have seen a surge in the availability of C-band Synthetic Aperture Radar (SAR) data due to the successful launches of Envisat ASAR in 2002, RADARSAT-2 in 2009, Sentinel-1 CSAR in 2014/2016, and the RADARSAT Constellation Mission (RCM) in 2019. In comparison to optical sensors, C-band SAR has the ability to penetrate through clouds and features day-and-night operability, making it an indispensable data source for the Earth Observation (EO) user community. Microwaves in the C-band frequency domain are highly responsive to the presence of water, allowing one to monitor bio-geophysical processes such as soil moisture [1,2], vegetation dynamics [3,4], snow melt [5,6], and flooding [7,8].

However, the side-looking acquisition geometry of SAR has the disadvantage of causing terrain distortions, which can only be corrected to a certain degree. A Digital Elevation Model (DEM) is a prerequisite to geolocate each observation correctly by using the well-established range-Doppler geocoding procedure. DEMs are also used to derive essential geometrical properties of SAR observations, e.g., the local incidence angle or the scattering area. These terrain characteristics are indispensable for transforming the measured radar brightness ( $\beta^0$ ) into the backscatter coefficients sigma nought ( $\sigma^0$ ) and gamma nought ( $\gamma^0$ ), which are based on models that approximate the surface as a collection of small, spherical scatterers [9,10].  $\gamma^0$  refers to the area perpendicular to the looking direction and is often the preferred quantity for a complex surface, since it remains constant for a perfectly rough surface or dense vegetation [11,12].

The orientation of the terrain with respect to the sensor significantly impacts the radiometry, since the size of the local illuminated area is one of the key components that govern the returned signal. Mitigating these radiometric distortions is essential to reveal the underlying signal of objects covering the terrain. Thus, several Radiometric Terrain Correction (RTC) methods have been developed to normalise backscatter data and to reduce their dependence on the looking direction. As an example, Ulander [13], Loew and Mauser [14], Hoekman et al. [12], and Vollrath et al. [15] presented geometric angular-based terrain slope and azimuth corrections using the local incidence ( $\theta/\theta_i$ ) and projection ( $\psi$ ) angle. However, these approaches apply a correction directly in map geometry and neglect the homomorphism between orbit and map geometry, which is taken into account by Small's radiometric terrain-flattening algorithm [16,17]. Small's RTC method directly utilises the local illuminated area of the sensor to normalise backscatter data in orbit geometry, which results in the so-called RTC gamma nought backscatter coefficient ( $\gamma_T^0$ ).  $\gamma_T^0$  is a major milestone on the road to analysis-ready SAR backscatter data and was, thus, chosen by the Committee on Earth Observation Satellites (CEOS) as the standard for Normalised Radar Backscatter (NRB) [18].

Several NRB products from various software packages have already been thoroughly validated and tested by Flores-Anderson et al. [19], demonstrating their superiority in undulated terrain and in densely vegetated regions.  $\gamma_T^0$  has also already proven beneficial for deriving higher-level products, e.g., forest and wet snow maps [20–22]. Substantial effort is needed to roll out NRB data production globally, since radiometric terrain correction is a time-consuming process [23]. Other backscatter coefficients like Geometric Terrain-Corrected (GTC) sigma nought ( $\sigma^0$ ) require fewer resources but clearly lack adequate radiometric quality in steeper terrain or when comparing backscatter between near and far ranges [19]. Regardless of the chosen coefficient or methodology for RTC, it is important to note that georeferencing and RTC operations are DEM-dependent, leading to an over- or under-compensation of the computed local illuminated area [14,16].

In addition to Small's RTC algorithm [17], Small et al. [24] proposed a method for generating wide-area, analysis-ready radar backscatter composites. By calculating a weighted average using the Local Contributing Area (LCA), preference is given to measurements with a higher local resolution. In steep terrain, the method allows for the combination of observations from different orbit directions considering the orientation of the terrain facets and automatically fills gaps caused by shadowing.

The RTC methods presented in the studies of Small et al. [16,17,24] and Loew and Mauser [14] only take into account the geometric component of the SAR acquisition, without considering the scattering properties of the target. Several publications have demonstrated the sensitivity of the C-band backscatter–incidence angle relationship to certain types of land cover [25–30]. For instance, backscatter from dense vegetation shows little dependence on the incidence angle due to a high volume-scattering contribution,

whereas water bodies act as mirrors, scattering the incoming radiation away from the sensor. Thus, when measurements from different orbits are aggregated, wherever a strong incidence angle dependence exists, systematic orbital artefacts emerge in the combined product.

Zhao et al. [31] and Villard et al. [32] extended the RTC standard, which is only based on the scattering area, by also correcting for polarisation-dependent scattering mechanisms of the land cover, such as differences caused by double bounce and volume scattering over vegetated areas. Both studies utilised polarimetric SAR data to perform a so-called Polarimetric Orientation Angle (POA) correction. Due to the correlation of the rotation of the polarisation ellipse with the azimuth angle, POA can be used to reduce azimuthal effects in the backscattering coefficient. Both studies confirmed that after POA-corrected measurements have been normalised by the local scattering area, it is still necessary to account for Angular Variation Effects (AVEs). Using an incidence angle-based cosine model [11] coupled with polarimetric information, both studies were able to minimise reflection asymmetry and incidence-angle dependence over forested areas. Chen et al. [33] focused on normalising backscatter data to a common reference angle over the Greenland ice sheet and resolved the issue of incidence-angle dependence by considering freeze-thaw-related factors.

However, these methods require polarimetric SAR data, sufficient orbital coverage, or auxiliary data and are optimised for one specific type of land cover. Generic and adequate modelling of the backscatter–incidence angle relationship is therefore key to being able to normalise backscatter to a common reference incidence angle, which mitigates the impact of incidence angle-dependent scattering for different types of land cover. Existing approaches utilise linear regression or first-order radiative transfer models on a dense time series of backscatter–incidence angle observations to describe this relationship with a slope value (first-order derivative) and, if possible, a curvature value (second-order derivative) [12,25,34–36]. Depending on the given satellite and acquisition strategy, observations from a multitude of different incidence angles may be limited, requiring a reduction in the complexity by assuming a linear relationship. Scatterometers like ASCAT offer simultaneous measurements in six different directions, whereas SAR sensors provide observations from only a single looking direction from distinct relative orbits.

At the forefront of modern SAR missions, Sentinel-1 stands out due to its high spatio-temporal resolution, stable orbit trajectory, and open data access policy [37]. To achieve a high and regular revisit time globally, Sentinel-1 revolves the Earth in 175 Sun-synchronous, relative orbits at a height of 700 km. This acquisition scheme, together with the observation scenario that gives preference to European land and tectonic areas, yields a limited set of measurements from different incidence angles [38]. With the majority of Earth's land surfaces only being covered by one orbit, it is impossible to use linear regression to calculate a slope value. Other studies working with GTC sigma nought backscatter used an average slope value for areas where it is not possible to calculate a slope [27] or introduced a multivariate linear regression model based solely on backscatter [35] or other auxiliary variables [33].

In this paper, our aim is to improve the current standard of analysis-ready SAR backscatter data by creating seamless, normalised radar backscatter composites. Building on the work of Bauer-Marschallinger et al. [35] and Hoekman et al. [12], we introduce a novel Machine Learning (ML)-based approach to estimate slope values from several  $\gamma_T^0$  backscatter statistics. This approach relies on the assumption that there is a correlation between backscatter statistics and the actual computed backscatter–incidence angle slope. Certain statistics, such as the average backscatter and the sensitivity (representative of the spread of the backscatter distribution), have been found to correlate well with the backscatter–incidence angle slope [35,39].

Since land cover effects prevail after correcting for geometric terrain illumination, the complexity of the relationship between backscatter and incidence angles increases. Thus, machine learning may help to estimate this relationship more reliably than a simple multivariate regression model when working with  $\gamma_T^0$  instead of  $\sigma^0$ . This novel approach enables the global availability of a  $\gamma_T^0$  backscatter–incidence angle slope to normalise backscatter data to a certain reference angle without being limited to well-covered regions.

Section 2.6 explains the design of the machine learning model in more detail. Our SAR pre-processing engine, *wizard*, which was developed in-house, was used to generate RTC gamma nought backscatter data cubes for several regions of interest around the world (Section 2.1.2). The statistical parameters derived from these data cubes (Section 2.4) were ingested into the machine learning model to train and estimate a slope value (Section 3.1). The estimated slope value was then used to normalise the backscatter data to a certain reference incidence angle, preferably to the mean incidence angle of Sentinel-1’s swath at around 38° [27]. Finally, we present the aggregated result of normalised backscatter time series as seamless radar backscatter composites in Sections 3.2 and 3.2.2.

## 2. Materials and Methods

### 2.1. Input Data

#### 2.1.1. Regions of Interest

Figure 1 provides a global overview of all 36 regions of interest for this study. The selection was performed based on the following criteria: (a) broad global coverage, (b) a diverse distribution of land cover types (Figure 1, bottom), and (c) consideration of the number of relative orbits (Figure 1, top). ESA’s WorldCover 2021 land cover dataset served as a reference to assign a land cover type to each data point [40]. The number of relative orbits was calculated from the GTC sigma nought data cube from Wagner et al. [41] for the years spanning 2019–2022. The global distribution shown in Figure 1 highlights the sparse multidirectional and multiorbital acquisition scheme of Sentinel-1 outside of Europe. Approximately half of global land surfaces are observed from more than one relative orbit. In particular, Africa and Oceania are only imaged from one orbit direction. Retrieving a slope value by applying linear regression on backscatter and incidence angles is therefore impossible for these regions and requires a different approach to obtain a reliable estimate.

The dots in Figure 1 (bottom) mark the regions of interest and are scaled by the average terrain slope derived from the 30 m Copernicus DEM [42]. Most of the regions are in rather flat or hilly terrain (0–20°), and a few are located in steeper terrain (>20°), e.g., in the Alps and the Himalayas.

Each region of interest has an extent of 100 × 100 km and is represented as a tile in the Equi7Grid system [43], which minimises distortions and oversampling, making this an optimal gridding and projection system for high-resolution raster data. All imagery were sampled at or resampled to 20 m following the datacube architecture reported in [41]. The following subsections provide more details on the input data generated for each tile defining a region of interest.

#### 2.1.2. RTC Backscatter

The key input for our experiments is RTC gamma nought backscatter derived from Sentinel-1 Ground Range Detected (GRD), Interferometric Wide (IW) swath data. Sentinel-1 IW GRD data were retrieved for the years 2019, 2020, and 2021 from the Earth Observation Data Centre for Water Resources Monitoring (EODC, [44]) storage and processed at the Vienna Scientific Cluster 5 (VSC-5, [45]). We specifically limited the time range of the input data to these years to (a) limit the impact of border and thermal noise, which was mitigated after the release of version 2.90 of the Instrument Processing Facility (IPF) software [46–48],

and (b) benefit from the dense observation time series from both satellites (Sentinel-1A and Sentinel-1B). Unfortunately, due to an anomaly in the instrument's power supply, Sentinel-1B stopped delivering radar data on 23 December 2021 [49].

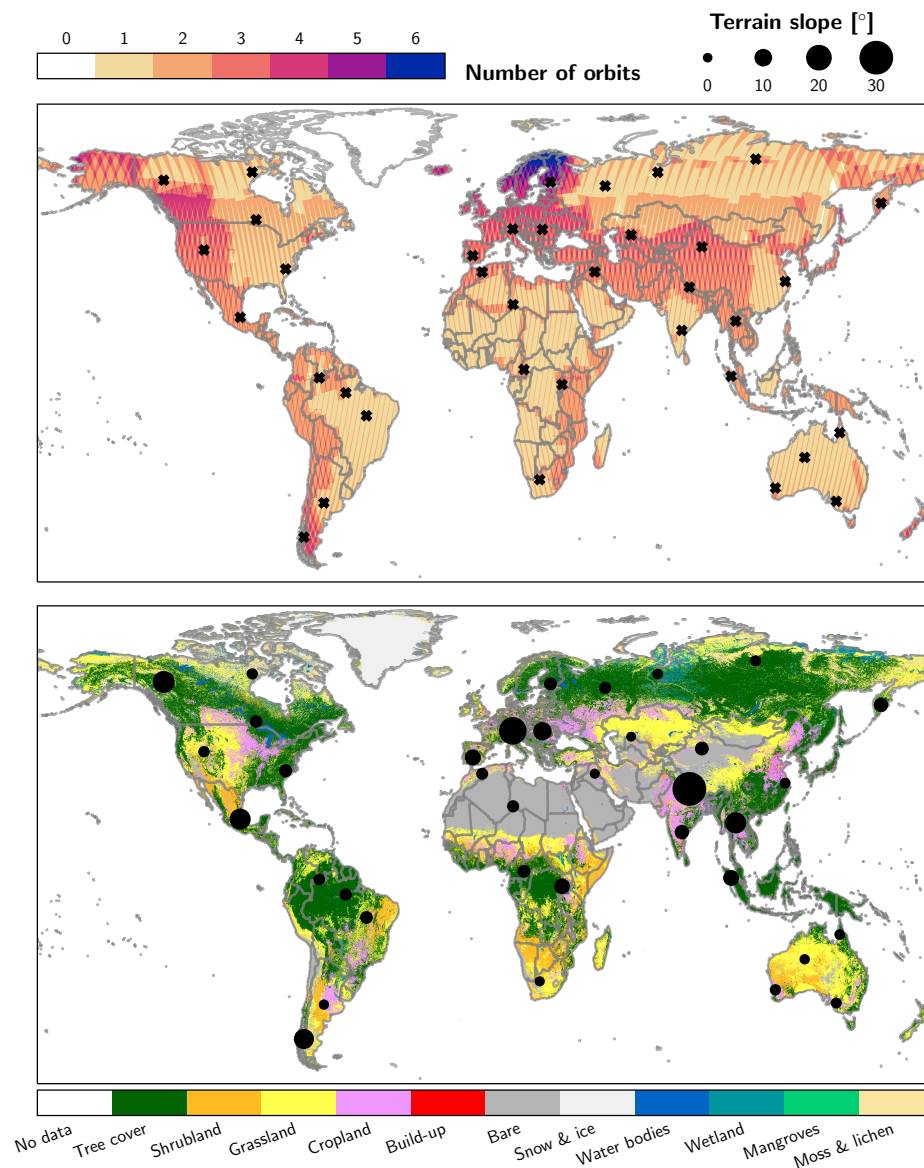


**Figure 1.** Number of relative orbits derived from Wagner et al. [41] (top) and ESA WorldCover 2021 [40] (bottom). All regions of interest are visible as black markers and are scaled by the average terrain slope in the lower figure. The crosses in the upper figure remain constant to avoid overlaying any interesting orbital patterns.

The total volume of input data of around 25 TB distributed across 25,000 files requires a significant amount of processing effort to perform radiometric terrain flattening and georeferencing. Our in-house-developed, efficient SAR pre-processing toolbox, *wizard* [23,50], alleviated the heavy lifting and enabled the production of RTC gamma nought backscatter. The processing chain utilising *wizard* is shown in Figure 2 and resembles the ones presented in [23,50]. We used the Copernicus DEM 30 m [42] for all map geometry and precise orbit data (POEORB [51]) for all orbit geometry operations.

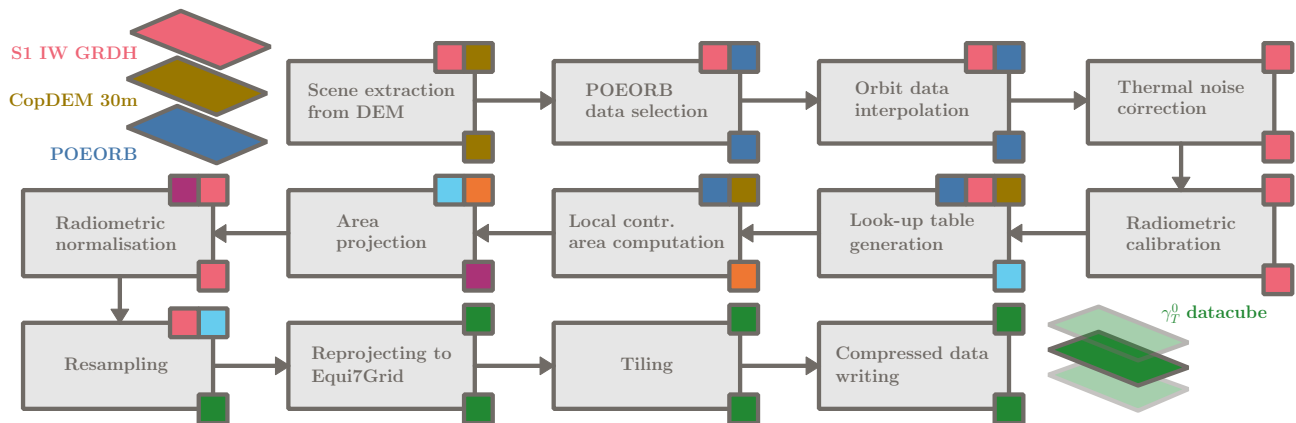


**Figure 2.** RTC gamma nought ( $\gamma_T^0$ ) pre-processing workflow implemented in *wizensard*. The grey boxes represent a specific processing step; the smaller boxes in the upper corner represent the input layers, and those in the lower corner represent the output layers. The colours of the small boxes help to trace the data flow of the processing chain. More details can be found in [23].

On top of the processing chain presented in [23], we added cubic-spline re-gridding of scene-based RTC backscatter data from the LatLon projection to tile-based data cubes with a 20 m sampling in the Equi7Grid system. The target sampling of 20 m not only drastically reduces the data volume but also diminishes the effect of speckle. *wizensard* still applied a scene-by-scene-based processing approach, where narrow gaps might occur between adjacent scenes of the same swath after georeferencing [27].

To obtain information on the viewing geometry necessary for estimating the backscatter–incidence angle relationship, the local incidence angle and the local contributing area per relative orbit were computed following the framework presented by Navacchi et al. [23,50]. In addition, *wizensard* was used to generate a static layover and shadow mask per relative orbit to remove artefacts originating from the side-looking data acquisition of the radar sensor [52].

## 2.2. Slope ( $\beta$ ) Computation

Within the limits of DEM accuracy and resolution, the generated  $\gamma_T^0$  data cubes show a significant reduction in the influence of the illuminated area on the backscattered signal [14,16]. The remaining systematic influence of the sensor’s viewing geometry after RTC is governed by the scattering characteristics of the land surface [53].  $\gamma_T^0$  resembles the scattering area-corrected data of Zhao et al. [31] and Villard et al. [32], who further normalised the data using polarimetric or aggregated backscatter–incidence angle correlation information over forested areas. However,  $\gamma_T^0$  from Sentinel-1 only provides dual-polarised measurements and a limited orbital coverage to model and utilise the backscatter–incidence angle relationship for normalisation. In general, complex spatio-temporal variations exacerbate the physical modelling of the backscatter–incidence angle relationship, which is therefore often simplified by a single linear slope coefficient ( $\beta$  [db/°]). Equation (1) defines this linear relationship specifically for the local incidence angle ( $\theta$ ) and RTC gamma nought ( $\gamma_T^0$ ).

$$\gamma_T^0(\theta) = \beta \cdot \theta + const. \quad (1)$$

$\beta$  is usually calculated directly from observation pairs ( $\theta$ ,  $\gamma_T^0$ ) using linear regression [35,39]. Scatterometers such as ASCAT offer concurrent measurements from various incidence angles (25–64°), enabling a reliable estimation of  $\beta$  [54]. However, the C-band sensor onboard Sentinel-1 observes Earth from a single looking direction and operates in 175 distinct relative orbits [37]. This yields a limited range of backscatter observations from different incidence angles, with a maximum coverage of six orbits over northern land

surfaces (Figure 1, top). Reliably computing the slope of the backscatter–incidence angle relationship is therefore challenging, given the narrow range (29–45° for the IW mode) and sparse set of incidence angles.

Due to these constraints, it is essential to mask areas where the following rules apply:

- Locations are only observed by one orbit, i.e., the linear system is under-determined;
- The relative standard error of the slope calculation should not exceed 5% with respect to the given incidence angles and the average incidence angle ( $\theta_0$ ) of 38° for Sentinel-1's IW mode, as formulated by the following equations [55]:

$$SE_{\gamma_T^0} = S_{\gamma_T^0 \cdot \theta} \cdot C \quad (2)$$

$$C = \sqrt{1 + \frac{1}{n} + \frac{(\theta_0 - \bar{\theta})^2}{SS_\theta}} \quad (3)$$

where  $SE_{\gamma_T^0}$  is the standard error of the linear regression,  $S_{\gamma_T^0 \cdot \theta}$  is the standard error of the estimate,  $n$  is the number of observations,  $\bar{\theta}$  is the average incidence angle, and  $SS_\theta$  is the sum of the squared error of  $\theta$ .  $C$  acts as a scale factor and can therefore be used to mask all pixels, where  $(C - 1) \cdot 100 > 5\%$ .

Following the rules outlined above ensures that only reliable slope data are used as a target variable for training the ML model.

Before calculating  $\beta$  for each pixel for all data between 2019 and 2022 using linear regression, the input was separated into each orbit direction to prevent the impact of azimuthal anisotropy. This effect is explained in more detail in [13,24,32,56] and was already heavily reduced by radiometric terrain correction. However, as visually demonstrated in Figure 3, some azimuthal effects remain in the slope and normalised data depending on the type of land cover. Figure 3 (top) shows a bias for certain fields, tree-lined roads, and urban areas, which were not radiometrically adjusted due to (a) insufficient detail of the digital elevation model and (b) land cover dynamics. In addition, we observed large slope differences between the ascending and descending overpasses for, e.g., the Bonneville Salt Flats in Utah, USA (Figure 3, bottom). Extensive flooding in the winter months and high diurnal temperature differences cause large variations in the aggregate state of water [57]. Sentinel-1 passes the Bonneville Salt Flats around 7.30 a.m./p.m. local time and, thus, observes different surface conditions, causing the slope bias in Figure 3 (bottom).

Finally,  $\beta$  can be used to correct for systematic changes in backscatter by calculating a normalised backscatter value [27,35]. Equation (4) explicitly formulates this correction using a reference incidence angle ( $\theta_0$ ) of 38°.

$$\gamma_T^0(\theta_0) = \gamma_T^0(\theta) - \beta \cdot (\theta - \theta_0) \quad (4)$$

The sparse orbital coverage of Sentinel-1 and the separation of different orbit directions result in measurements from only one or two distinct incidence angles for all regions of interest. Thus, the limited set of incidence angles prevents the usage of a non-linear model representing the backscatter–incidence angle relationship and hinders the quantification of non-linear effects, where our basic assumption of a linear model would not be applicable.

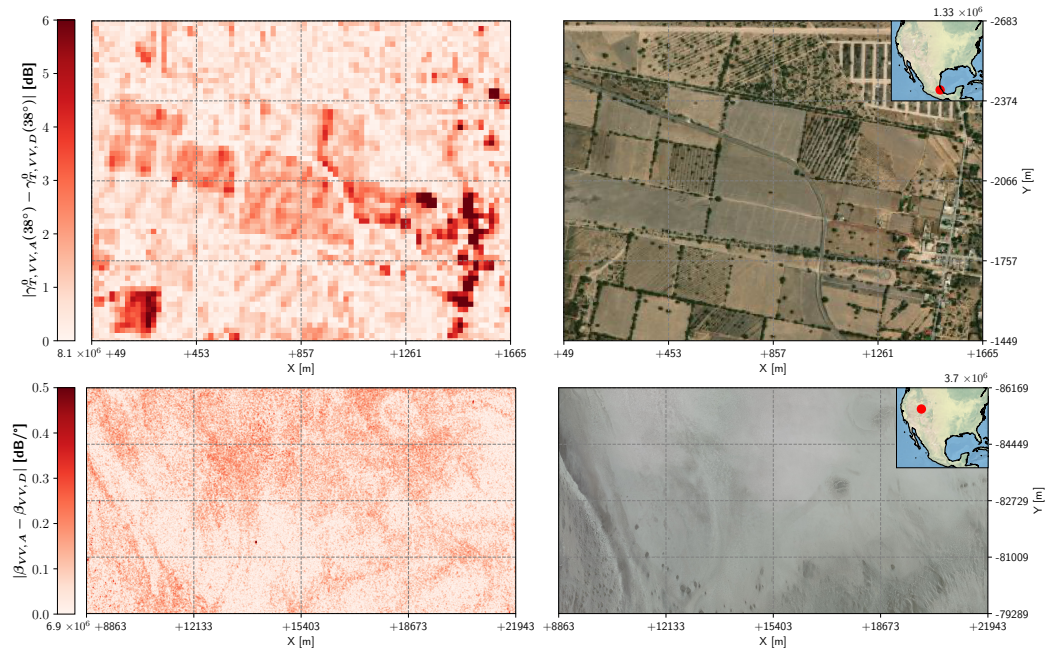


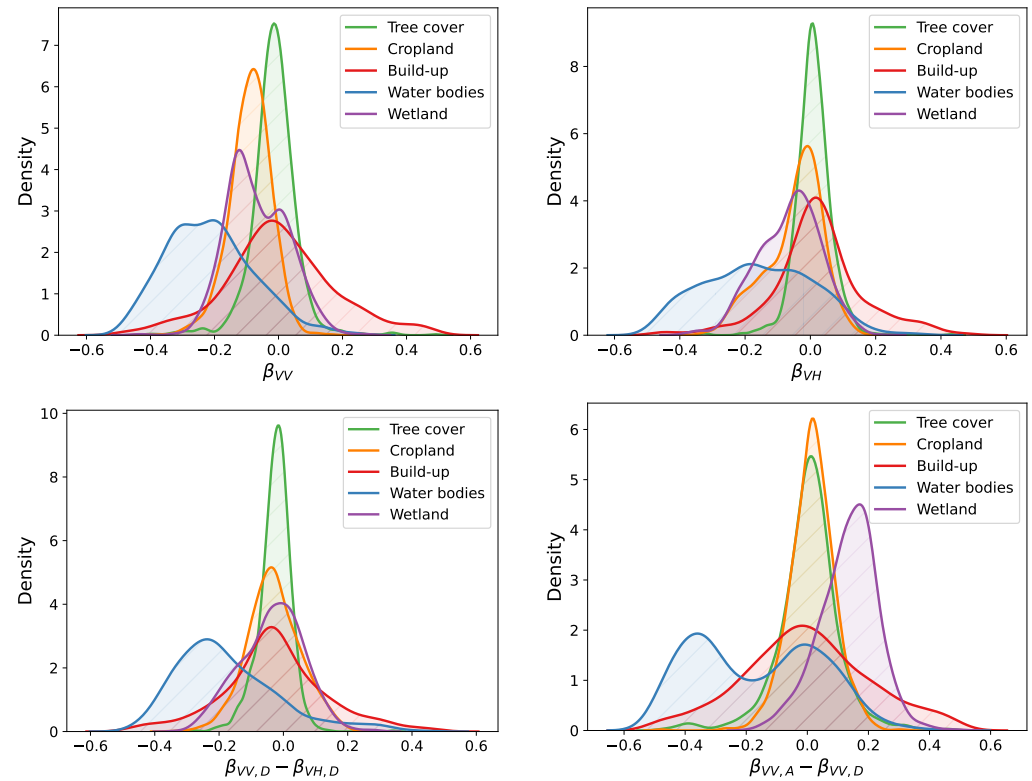
**Figure 3.** Orbit direction difference of normalised  $\gamma_T^0$  ( $\gamma_T^0(38^\circ)$ , **top left**) and  $\beta$  computed from VV polarised  $\gamma_T^0$  ( $\beta_{VV}$ , **bottom left**). Optical imagery (©2024 Microsoft Corporation, ©2024 Maxar, ©CNES (2024), ©Earthstar Geographics SIO) is provided in the second column.

### 2.3. Slope Analysis

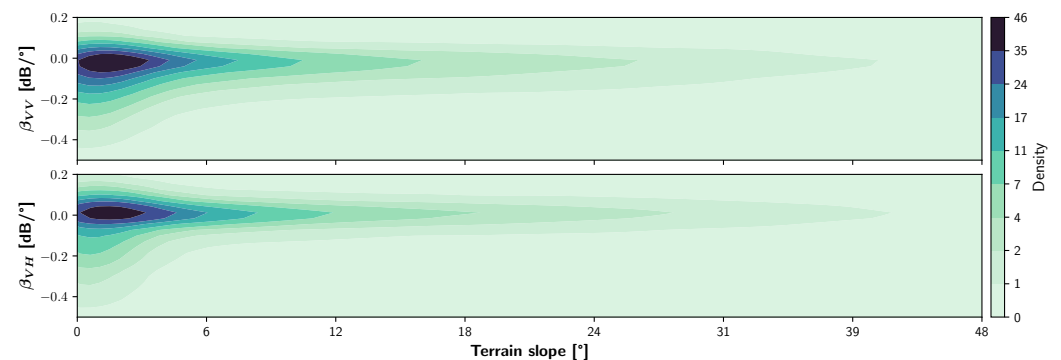
In this section, we briefly present the behaviour of  $\beta$  with respect to different land cover types covered by our regions of interest. Figure 4 shows distributions of  $\beta$  for different polarisations, orbit directions, and land cover types. The distributions are based on all data points that meet the requirements explained in Section 2.2, providing a reliable slope value. Comparing  $\beta_{VV}$  with  $\beta_{VH}$  shows the pronounced scattering characteristics of VV polarised backscatter for all land cover types. Due to specular reflections, backscatter from *water bodies* experiences the most significant dependence on the incidence angle and polarisation (Figure 4, bottom left). Volume scattering prevails for *tree cover*, which is a slim distribution centred around zero. This fulfils the expected behaviour of  $\gamma^0$  [11,58,59] and implicitly confirms the excellent performance of RTC gamma nought backscatter as already presented in other studies [19,20]. The non-central *wetland* and *water bodies* distributions in Figure 4 (bottom right) demonstrate the necessity of separating different orbit directions, as already explained in Section 2.2. In addition to *wetland*, backscatter from *water bodies* is heavily impacted by the orbit direction, which is also likely caused by the difference in local time and the state of the water during Sentinel-1's overpasses. *Built-up* areas show up as a zero-centred, broad distribution in every plot, indicating complex angular behaviour due to double-bounce effects or specular reflections [60].

Figure 5 provides further insights into the behaviour of the slope values for each polarisation with respect to the terrain slope. As already indicated by Figure 1 (bottom), the largest portion of the terrain slope is between  $0^\circ$  and  $10^\circ$ . In this flat terrain, the slope values spread over the full range shown in Figure 4, whereas for higher terrain slopes, the distribution approaches  $\beta = 0$ . The VH distribution is narrower than the VV distribution, which shows that  $\beta_{VH}$  is less affected by the terrain slope than  $\beta_{VV}$  and might be linked to the presence of forests in steeper terrain [29]. Overall, Figure 5 confirms that RTC mitigates the impact of the terrain (slope). Additionally, certain land cover in flat terrain, e.g., water bodies causing strong forward scattering, clearly has more impact on the RTC backscatter–incidence angle relationship than the terrain slope.

Considering a steepest slope of  $-0.5 \text{ dB}/^\circ$ , Sentinel-1's incidence-angle range of  $29\text{--}47^\circ$ , and a reference incidence angle of  $38^\circ$ , the actual difference between normalised and non-normalised backscatter is around 5 dB. The magnitude of this difference indicates that land cover significantly affects  $\gamma_T^0$ , and normalising for incidence angle is essential when merging data from various orbits.



**Figure 4.** Slope distributions for VV polarised  $\gamma_T^0$  ( $\beta_{VV}$ , **top left**), VH polarised  $\gamma_T^0$  ( $\beta_{VH}$ , **top right**), their difference (**bottom left**), and the difference between the two orbit directions ( $\beta_{VV,A} - \beta_{VV,D}$ ) (**bottom right**) for the land cover classes *tree cover*, *cropland*, *built-up*, *water bodies*, and *wetland*.



**Figure 5.** Two-dimensional distributions of the terrain slope and the computed slope values ( $\beta$ ) for VV (**top**) and VH (**bottom**) polarisation.

#### 2.4. Parameter Generation

Following the approach of Bauer-Marschallinger et al. [35], our objective is to model  $\beta$  as a function of various statistical parameters derived from  $\gamma_T^0$  backscatter instead of parameterising it directly via the incidence angle. Estimating  $\beta$  without being dependent on the incidence angle facilitates the normalisation of backscatter data to a standardised reference angle, since issues with an under-determined system of equations are prevented upfront. Finding parameters that are sensitive to the behaviour and variations of  $\beta$  (Section 2.3) is,

thus, indispensable before modelling  $\beta$  using machine learning. Wagner et al. [39] and O’Grady et al. [28] have already pointed out several statistics showing a noticeable correlation with  $\beta$ : the average backscatter and the (static) sensitivity, defined as the difference between maximum and minimum backscatter values. The additional advantage is that these statistical parameters are less noisy and less impacted by the acquisition scheme than the actual computed slope [35]. The RTC  $\gamma_T^0$  backscatter data cubes served as a basis to extract various statistical parameters that represent a broad range of slope conditions. All parameters considered as input data for training the ML model presented in Section 2.6 are listed below (generated for each orbit direction):

- Mean of  $\gamma_T^0$  ( $\bar{\gamma}_T^0$ ) for each polarisation;
- The 5th and 95th percentiles of  $\gamma_T^0$  for each polarisation;
- The difference between the  $\gamma_T^0$  percentiles (referring to sensitivity from now on [35]) for each polarisation ( $\tilde{\gamma}_T^0$ );
- Mean of the Cross-Ratio (CR)  $\gamma_{T,CR}^0$  ( $\bar{\gamma}_{T,CR}^0$ );
- The 5th and 95th percentiles of  $\gamma_{T,CR}^0$ ;
- The difference between the  $\gamma_{T,CR}^0$  percentiles ( $\tilde{\gamma}_{T,CR}^0$ ).

Figure 6 visualises a subset of these parameters for a small region containing all kinds of land cover. Each parameter is able to highlight a certain set of features. Vegetation stands out in the VH parameters and, consequently, in the CR parameters as well [59,61]. Due to a high volume-scattering contribution for larger incidence angles and, thus, a slope close to zero (Figure 4), the sensitivity ( $\tilde{\gamma}_T^0$ ) is the lowest compared to other land cover types.

The finest granularity of grasslands and croplands is present for all sensitivity parameters, making it possible to identify field boundaries and agricultural patterns. A very dominant feature is the small water body/wetland in the top-left corner of the area. A low average backscatter and a high sensitivity indicate forward scattering with a steeper slope. In addition, the water surface is observed at high incidence angles, causing a stronger contribution of the horizontal component to the backscattered radiation and, thus, a higher CR [59]. The provided points make it clear that this collection of parameters is suitable for characterising various conditions of  $\beta$ .

### 2.5. $\beta$ Uncertainty

Information on the uncertainty of the slope values is indispensable for assessing the performance of the ML model and highlighting areas or specific types of land cover that are a priori difficult to model. In addition to the parameters described in Section 2.4, we calculated the standard deviation of  $\gamma_T^0$  based on a log-normal distribution for each relative orbit ( $o$ ) (Equation (5)):

$$\sigma_{\gamma_T^0}^2(o)[\text{dB}] = \ln \left( 1 + \frac{\overline{\gamma_T^0}^2(o)}{\sigma_{\gamma_T^0}^2(o)} \right) \quad (5)$$

where  $\sigma_{\gamma_T^0}^2(o)$  is the variance of  $\gamma_T^0$  in linear units for each relative orbit and  $\sigma_{\gamma_T^0}^2(o)$  [dB] is the respective variance in dB. Inserting this, together with the incidence-angle difference ( $\Delta\theta$ ), into Equation (6) yields the standard deviation of the slope ( $\sigma_\beta$ ). Since most of the slopes were calculated based on input data from two relative orbits, Equation (6) was derived using Gaussian uncertainty propagation starting from a (two-point) linear model with  $\beta$  as an unknown.

$$\sigma_\beta = \frac{1}{\Delta\theta} \cdot \sqrt{\sum_{o=0}^1 \sigma_{\gamma_T^0}^2(o)} \quad (6)$$

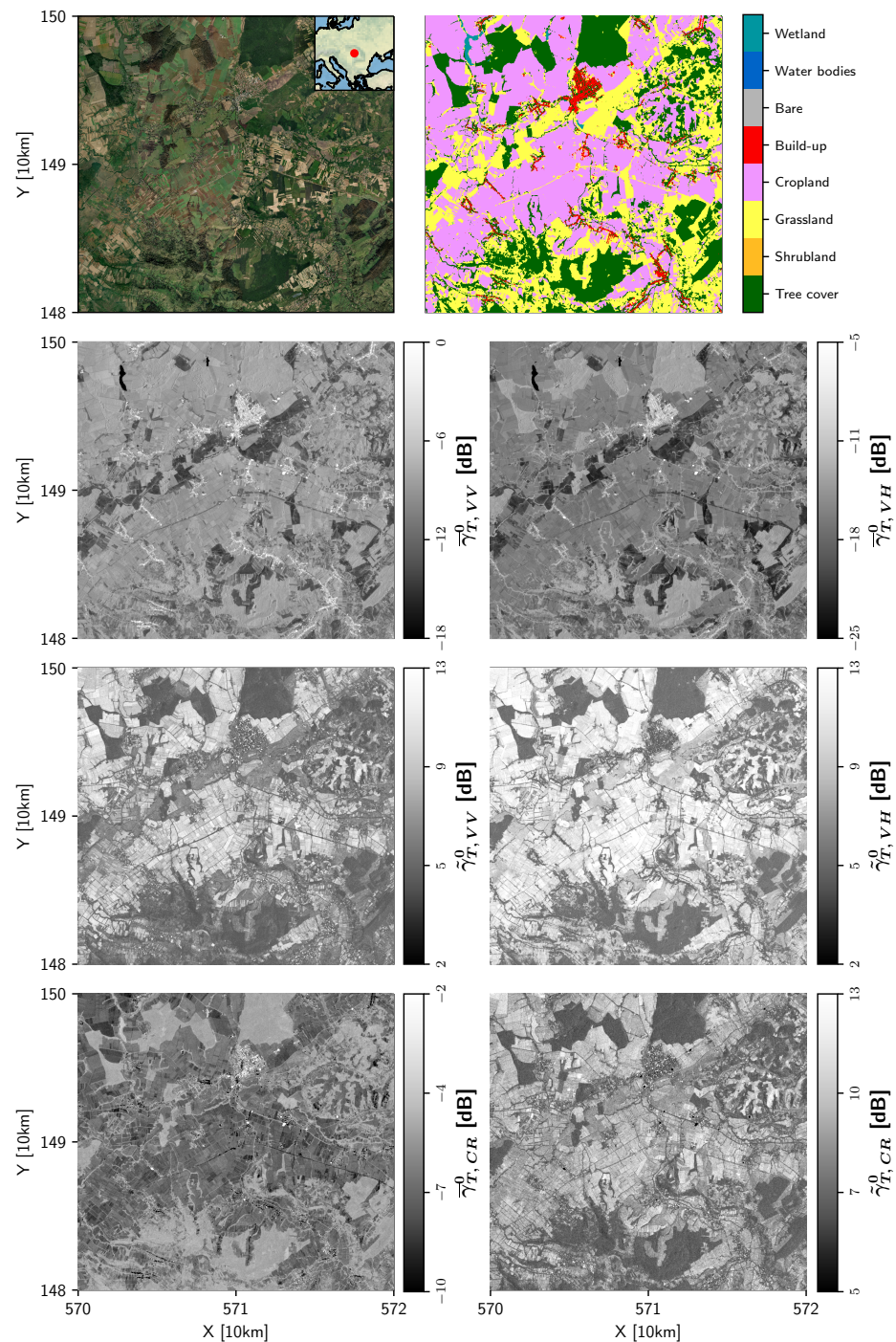


**Figure 6.** Input parameters for estimating  $\beta$  for each polarisation: mean of  $\gamma_T^0$ ,  $\tilde{\gamma}_T^0$  (VV, top left; VH, top right; CR, bottom left) and the percentile difference of  $\gamma_T^0$ ,  $\tilde{\gamma}_T^0$  (VV, centre left; VH, centre right; CR, bottom right). In this example, all input data were acquired from a descending orbit and cover the surroundings of the village of Marghita in Romania. To provide some context, the top row shows optical imagery (©2024 Microsoft Corporation Earthstar Geographics SIO) next to land cover data taken from ESA WorldCover 2021 [40].

Table 1 lists  $\sigma_\beta$  for each polarisation and for each type of land cover covered by two relative orbits. The expected range of slope values presented in Figure 4 indicates that  $\sigma_\beta$  is relatively high, especially for land cover types with significant temporal variability, such as water bodies (impacted by wind and a frozen surface), wetlands, and snow. Moreover, the 20 m sampling does not fully suppress the impact of speckle, further increasing the standard deviation.

**Table 1.** Estimated standard deviation of the slope for VV ( $\sigma_{\beta, \text{VV}}$ ) and VH ( $\sigma_{\beta, \text{VH}}$ ) polarisation for selected land cover types.

Land Cover	Tree Cover	Shrub-Land	Grass-Land	Built-Up	Bare	Water Bodies	Wetland	Cropland	Snow and Ice	Moss and Lichen
$\sigma_{\beta, \text{VV}}$ [dB/°]	0.4431	0.3604	0.5658	0.4093	0.6280	0.7798	0.6490	0.5073	1.1822	0.6372
$\sigma_{\beta, \text{VH}}$ [dB/°]	0.4810	0.4048	0.6393	0.3595	0.5946	0.4382	0.4469	0.5784	1.3447	0.7073

## 2.6. Machine Learning

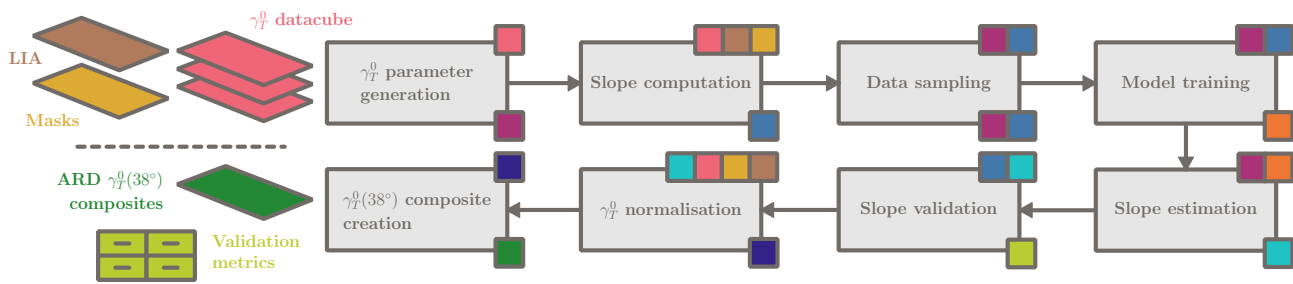
To account for the different scattering behaviours of co- and cross-polarised backscatter outlined in Section 2.3, distinct models were trained for both polarisations. Considering the large amount of input data and that the relation between the input variables and the target variable ( $\beta$ ) is assumed to be non-linear, a Neural Network (NN) was chosen as a model [62]. In the process of a randomised grid search, the ideal hyperparameters were identified. The resulting model was a Feed-Forward Neural Network (FFNN) with four hidden layers, starting with 58,000 neurons in the first layer, decreasing the number with every following layer by 25%. This led to a total of 145,000 neurons. Each hidden layer was followed by a *LeakyReLU* activation and a dropout layer as a regularisation mechanism to prevent overfitting. For the final dense layer, a linear activation function was used. *Adam* was selected as the optimiser, and *log cosh* was used as a loss function.

Figure 4 shows that the slope values accumulate near zero. Applying random sampling to generate input data for training of the model would, thus, lead to certain land cover types being under-represented, e.g., water bodies. To account for this, we performed two sampling strategies:

- (A) Balancing the land cover frequency by applying stratified sampling, i.e., we randomly selected an equal amount of data for each land cover type;
- (B) Balancing the slope frequency by applying stratified sampling, i.e., we randomly selected an equal amount of data for certain slope bins.

In total, 200,000 data points were collected from all regions of interest. Of these points, 4/5 were used for training and 1/5 for the validation of the model. Both model training and prediction were carried out on an NVIDIA A40 GPU node on the VSC-5.

Figure 7 composes all important steps of this study, which are explained in detail in the previous subsections. The  $\gamma_T^0$  data cubes are the main output of Figure 2 and are filtered for each polarisation and orbit direction. The subset of the  $\gamma_T^0$  data cubes serves as input for Figure 7, along with several auxiliary layers, like a SAR terrain mask and local incidence angles. The final outputs of the study are Analysis-Ready Data (ARD) radar backscatter composites aggregated from normalised  $\gamma_T^0$  time series and validation metrics derived by comparing the computed slope ( $\beta_r$ ) with the estimated slope ( $\beta_e$ ).



**Figure 7.** Workflow summarising all key components of our study. The grey boxes represent a specific processing step; the smaller boxes in the upper corner represent the input layers, and those in the lower corner represent the output layers. The colours of the small boxes help to trace the data flow of the processing chain. The whole workflow is executed separately for each polarisation and orbit direction.

### 3. Results

#### 3.1. Slope Estimations

The trained models were used to obtain a slope estimate ( $\beta_e$ ) for each combination of polarisation and orbit direction (VV-A, VV-D, VH-A, and VH-D) for all regions of interest. Valid reference slope values ( $\beta_r$ ) were extracted where none of the rules described in Section 2.2 apply and which were not used during the training phase. These values were compared to the estimated slope values ( $\beta_e$ ) using several accuracy metrics, which are compiled in Table 2 for each land cover type. The following results are based on the models trained with sampling strategy A, since the derived accuracy metrics did not deviate significantly.

Overall, RMSE values are high compared to the actual range of  $\beta$  in Figure 4. The MAE is significantly lower, which indicates the presence of larger differences, forcing the RMSE up. The highest values for both metrics can be observed for the land cover classes *snow and ice*, *bare*, *built-up*, and *water bodies*. When comparing the two polarisations, both metrics are lower for VH, which is due to the lower average slope of VH (c.f., Figure 4). Except for *wetland*, the relative behaviour of both metrics remains the same.

The averages of  $\beta_r$  ( $\overline{\beta_r}$ ) and  $\beta_e$  ( $\overline{\beta_e}$ ) tend to be close, with some larger discrepancies for *bare*, *built-up*, *snow and ice*, and *water bodies*. Wetland areas are well-estimated by the VH model, but  $\overline{\beta_r}$  significantly differs from  $\overline{\beta_e}$  in the case of the VV model. Moreover, for most land cover types, there is a trend according to which  $\overline{\beta_e}$  values are lower than  $\overline{\beta_r}$ , suggesting that both models are unable to estimate steeper slope values. This is further emphasised by the actual stretch of the slope distributions—represented by the inter-decile range—being fundamentally lower for the estimated slope values.

In the end, the estimated slope value ( $\beta_e$ ) is used to normalise backscatter data to a certain reference incidence angle [35]. To avoid introducing artefacts or improperly adjusting backscatter values, it is crucial that  $\beta_e$  exhibits a smooth behaviour and does not exceed  $\beta_r$ . Given that the backscatter–incidence angle relationship is linear, having  $\beta$  close to zero results in minimal modifications of the initial backscatter values. To assess this behaviour, we introduced an additional metric,  $\beta_{r\{e\}}$ , which sets  $\beta_e$  into direct relation with  $\beta_r$  and its average ( $\overline{\beta_r}$ ) as formulated in Equation (7).

$$\beta_{r\{e\}} = \frac{\sum_{i=0}^n (\text{sign}(\beta_{r,i} - \overline{\beta_r}) \cdot \text{sign}(\beta_{r,i} - \beta_{e,i}))}{n} > 0 \quad (7)$$

On average,  $\beta_{r\{e\}}$  is around 80%, which means the majority of  $\beta_e$  underestimates  $\beta_r$  but is still on the same level as the expected mean slope behaviour ( $\overline{\beta_r}$ ). Thus, by applying  $\beta_e$  instead of  $\beta_r$  to normalise backscatter data, the actual backscatter correction is softer and limits the presence of unpredictable and noisy artefacts. Statistics like RMSE and MAE,

as presented in Table 2, are clearly affected by the noisy behaviour of  $\beta_r$ , which can be partially justified with the high standard deviations ( $\sigma_\beta$ ) shown in Table 1.

**Table 2.** Accuracy metrics of calculated slope values ( $\beta_r$ ) and estimated slope values ( $\beta_e$ ) for selected land cover types: Root Mean Squared Error (RMSE), Mean Average Error (MAE), average reference slope ( $\bar{\beta}_r$ ), average estimated slope ( $\bar{\beta}_e$ ), Inter-Decile Range (IDR) for the reference slope ( $\text{IDR}(\beta_r)$ ), inter-decile range for the estimated slope ( $\text{IDR}(\beta_e)$ ), and the percentage of estimated slope values within the half-sided distribution limits of the reference slope values ( $\beta_{r\{e\}}$ , c.f., Equation (7)).

Land Cover	RMSE [dB/°]	MAE [dB/°]	$\bar{\beta}_r$ [dB/°]	$\bar{\beta}_e$ [dB/°]	$\text{IDR}(\beta_r)$ [dB/°]	$\text{IDR}(\beta_e)$ [dB/°]	$\beta_{r\{e\}}$ [%]
<b>VV</b>							
Tree cover	0.0900	0.0490	−0.0179	−0.0200	0.5520	0.0648	92.0
Shrubland	0.0735	0.0483	−0.0138	−0.0277	0.3328	0.0958	90.1
Grassland	0.1142	0.0638	−0.0637	−0.0539	0.6672	0.0643	81.4
Built-up	0.2686	0.1718	0.0065	−0.0476	0.6909	0.4245	88.1
Bare	0.1374	0.0913	−0.1246	−0.1158	0.4958	0.0961	79.8
Water bodies	0.1160	0.0860	−0.2147	−0.1846	0.1429	0.1114	77.9
Wetland	0.1342	0.0947	−0.0649	−0.1373	0.0722	0.0176	69.3
Cropland	0.0688	0.0459	−0.0866	−0.0722	0.1749	0.0443	81.6
Snow and ice	0.2053	0.1124	−0.1625	−0.1176	0.9971	0.3199	75.3
Moss and lichen	0.1230	0.0682	−0.1280	−0.0916	0.6406	0.0737	74.6
<b>Total</b>	0.1080	0.0617	−0.0604	−0.0561	0.6406	0.0737	77.5
<b>VH</b>							
Tree cover	0.0791	0.0436	0.0091	0.0050	0.4428	0.0306	93.5
Shrubland	0.0658	0.0447	0.0218	0.0039	0.2556	0.1393	85.6
Grassland	0.0974	0.0561	−0.0148	−0.0171	0.4682	0.0854	82.9
Built-up	0.1909	0.1172	0.0187	−0.0023	0.6476	0.1214	92.2
Bare	0.1142	0.0783	−0.1179	−0.0853	0.2472	0.0667	68.7
Water bodies	0.1165	0.0878	−0.1578	−0.1201	0.1005	0.0574	71.3
Wetland	0.0526	0.0403	−0.0645	−0.0628	0.0701	0.1112	70.8
Cropland	0.0709	0.0526	−0.0508	−0.0247	0.0884	0.0292	72.3
Snow and ice	0.1901	0.1129	−0.0946	−0.0489	0.8003	0.1084	76.5
Moss and lichen	0.1002	0.0615	−0.0488	−0.0246	0.5082	0.0935	80.9
<b>Total</b>	0.0933	0.0557	−0.0266	−0.0211	0.5082	0.0935	78.9

Figure 8 provides additional context by displaying the two-dimensional distributions of the reference slope ( $\beta_r$ ) and each input parameter (Section 2.4), as well as those of  $\beta_r$  and the estimated slope ( $\beta_e$ ). All input parameter distributions show the highest separability of water bodies with respect to other land cover types, which appear to be less correlated but also less stretched.  $\tilde{\gamma}_{T,CR}^0$  is characterised by the lowest value range and correlation with  $\beta_r$ , while  $\tilde{\gamma}_{T,VV}^0$  experiences a pronounced relation with  $\beta_r$ . The bottom row shows that the distributions are squeezed towards zero along  $\beta_e$ , leading to a wider range of  $\beta_r$  values compared to a smaller range of  $\beta_e$  values, which was already captured by  $\beta_{r\{e\}}$ .

Water bodies seem to correlate better and wetlands the least. This is probably caused by the insensitivity of wetlands present in the input data to  $\beta_r$ , since the same slope value covers almost the entire range of the sensitivity ( $\tilde{\gamma}_T^0$ ).

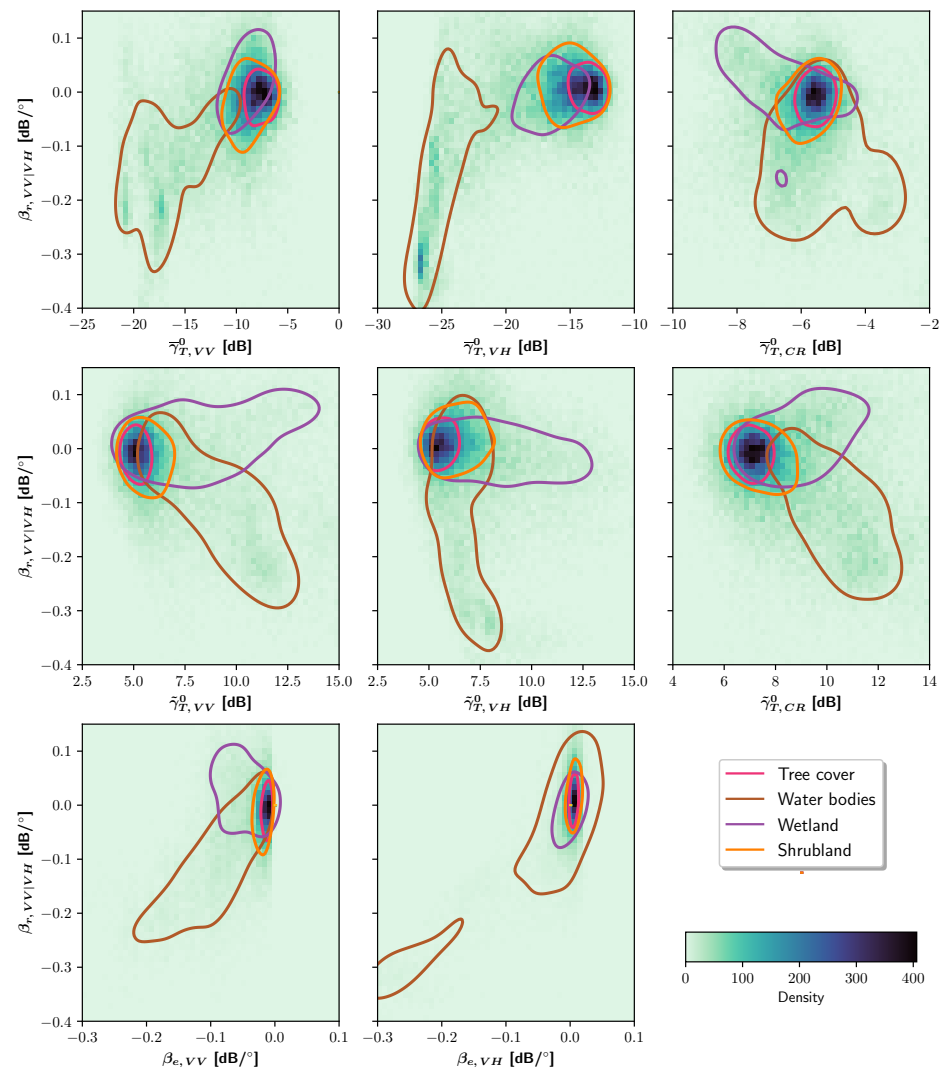


**Figure 8.** Two-dimensional distributions of the reference slope ( $\beta_r$ ) and each input parameter, i.e., the average  $\bar{\gamma}_T^0$  and sensitivity  $\tilde{\gamma}_T^0$  for each polarisation (and CR), as well as those of the reference slope ( $\beta_r$ ) and the estimated slope ( $\beta_e$ ). Contours show the 50% level of the kernel density estimate for *tree cover*, *water bodies*, *wetland*, and *shrubland*.

As an example to visually demonstrate the performance of the estimated slope value, Figure 9 compares the calculated reference slope values ( $\beta_r$ ) with the estimated ones ( $\beta_e$ ) for the same area of interest as in Figure 6. Overall,  $\beta_r$  and  $\beta_e$  show good agreement, as the land cover patterns are consistent. Higher slope values, i.e., close to zero, are visible for land surfaces covered by vegetation, e.g., tree cover, or anthropogenic objects, whereas lower slope values are present for water bodies and wetlands.  $\beta_e$  shows a smoother and more uniform appearance, whereas  $\beta_r$  is quite noisy, making it difficult to discern land cover transitions.  $\beta_e$  is based on multi-temporal statistics, which reduce the impact of noise, whereas  $\beta_r$  is directly influenced by speckle and the temporal variability of the land surface. The slope estimates from both ML models (VV and VH) appear to capture the overall slope behaviour effectively. For example, water bodies are more pronounced than other land cover types when comparing  $\beta_{e,VH}$  with  $\beta_{e,VV}$  (c.f., Figure 4), which could be due to the

fact that cross-polarised backscatter is less affected by wind ripples [63]. Another benefit of  $\beta_e$  over  $\beta_r$  is that the influence of corner reflectors on adjacent pixels is clearly mitigated.

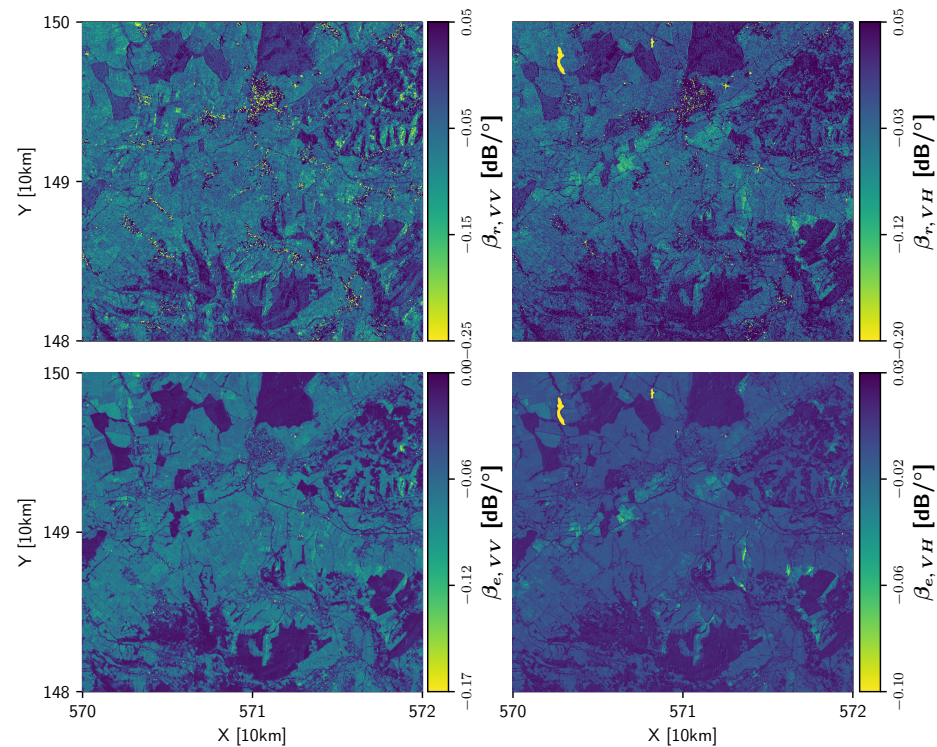


**Figure 9.** Calculated reference slope values ( $\beta_r$ ) for VV (top left) and VH (top right) polarisation and estimated slope values ( $\beta_e$ ) for VV (bottom left) and VH (bottom right) polarisation. The image content covers the same region of interest as in Figure 6. Attention should be paid to the varying scales of the colour bars.

In the northeastern and southern part of  $\beta_r, VV$ , some terrain-related effects appear. The orientation of the forested and farmed slopes with respect to the sensor might cause a difference in volume or double-bounce scattering [29], supported by the fact that they are not visible in the cross-polarised case, i.e.,  $\beta_r, VH$ . For both estimated slopes, these effects were completely removed.

Although  $\beta_e$  and  $\beta_r$  are relatively well-aligned, there appears to be a discrepancy in their absolute values shown by the two-dimensional distributions in the bottom row of Figure 8. In particular, for  $\beta_e, VH$ , the majority of land cover types exhibit higher slope values compared to  $\beta_r, VH$ , with most slope values being close to zero. The gap is significantly smaller in cases of  $\beta_r, VV$  and  $\beta_e, VV$  due to a higher sensitivity of VV polarised backscatter to surface scattering.

### 3.2. Backscatter Normalisation

Using the complete set of parameters (Section 2.4) as input for the model described in Section 2.6, we generated slope values ( $\beta_e$ ) for all regions of interest.  $\beta_e$  was then inserted into Equation (4) to generate normalised, radiometric terrain-corrected backscatter ( $\gamma_T^0$ ) at 38°. Figure 10 shows the distributions of non-normalised ( $\gamma_T^0$ ) and normalised ( $\gamma_T^0(38^\circ)$ ) backscatter for certain land cover types within nine regions of interest. For nearly all land cover types, the distributions are narrower after normalising the backscatter data. Depending on the magnitude of  $\beta$ , as visualised in Figure 4, the impact of normalisation increases from *tree cover* to *water bodies*. Notably, the backscatter from *water bodies* in “AS20M\_E026N015T1”, “AF20M\_E066N050T1”, and “AF20M\_E077N089T1” results in a

bimodal distribution. This phenomenon arises due to the presence of strong forward scattering and the dual orbital coverage of the tile. Normalising backscatter data transforms these bimodal distributions to bell-shaped distributions, with a significantly lower standard deviation and a mean value centred between the two peaks of the original distributions. This effect is also clearly visible for other land cover types, like wetlands and shrublands.

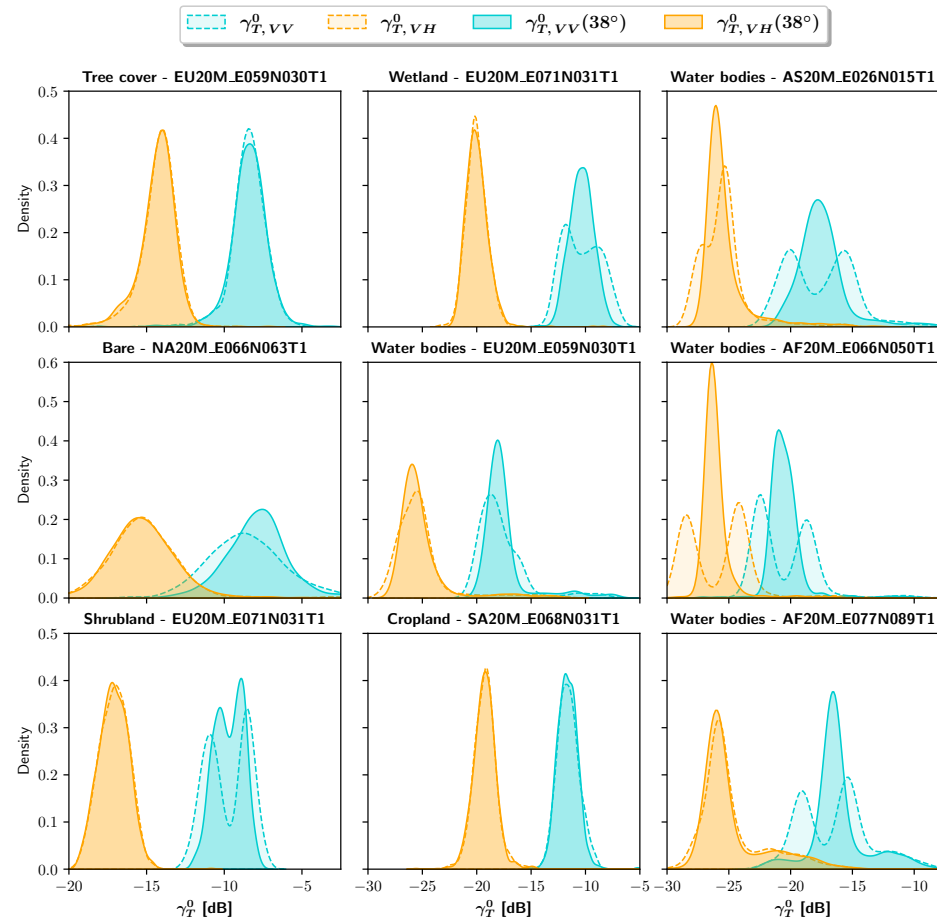


**Figure 10.** Comparison between non-normalised ( $\gamma_T^0$ ) and normalised ( $\gamma_T^0(38^\circ)$ ) backscatter distributions for each polarisation and a selection of land cover types in certain regions of interest. VV polarised backscatter is coloured as turquoise and VH polarised backscatter as orange. Non-normalised backscatter is shown in the background with a dashed contour. The reference to each region of interest originates from the Equi7Grid tile naming scheme [64].

### 3.2.1. Normalised Backscatter Composites

In order to create seamless normalised radar backscatter composites, we computed the temporal average of the  $\gamma_T^0(38^\circ)$  time series for each pixel for the period 2019–2022.

Figure 11 displays these composites in VV and VH polarisation for some selected areas in our regions of interest. In comparison to the non-normalised composites, all normalised composites show a significant improvement, with reduced orbital artefacts along the transitions of different swaths. Normalised composites covering the arid area in Iraq (second row), the wetlands in the Arctic tundra (fourth row), and the glacier in southern Chile (fifth row) appear completely seamless. For the other regions, slight orbital patterns are still visible. The agricultural areas in southern Australia (first row) show up smoother in the VV composite, whereas the opposite is the case for Lake Tai Hu in eastern China (third row). Notably, both normalised radar composites of Lake Tai Hu introduce new objects, which are not as visible or pronounced in the non-normalised composite.

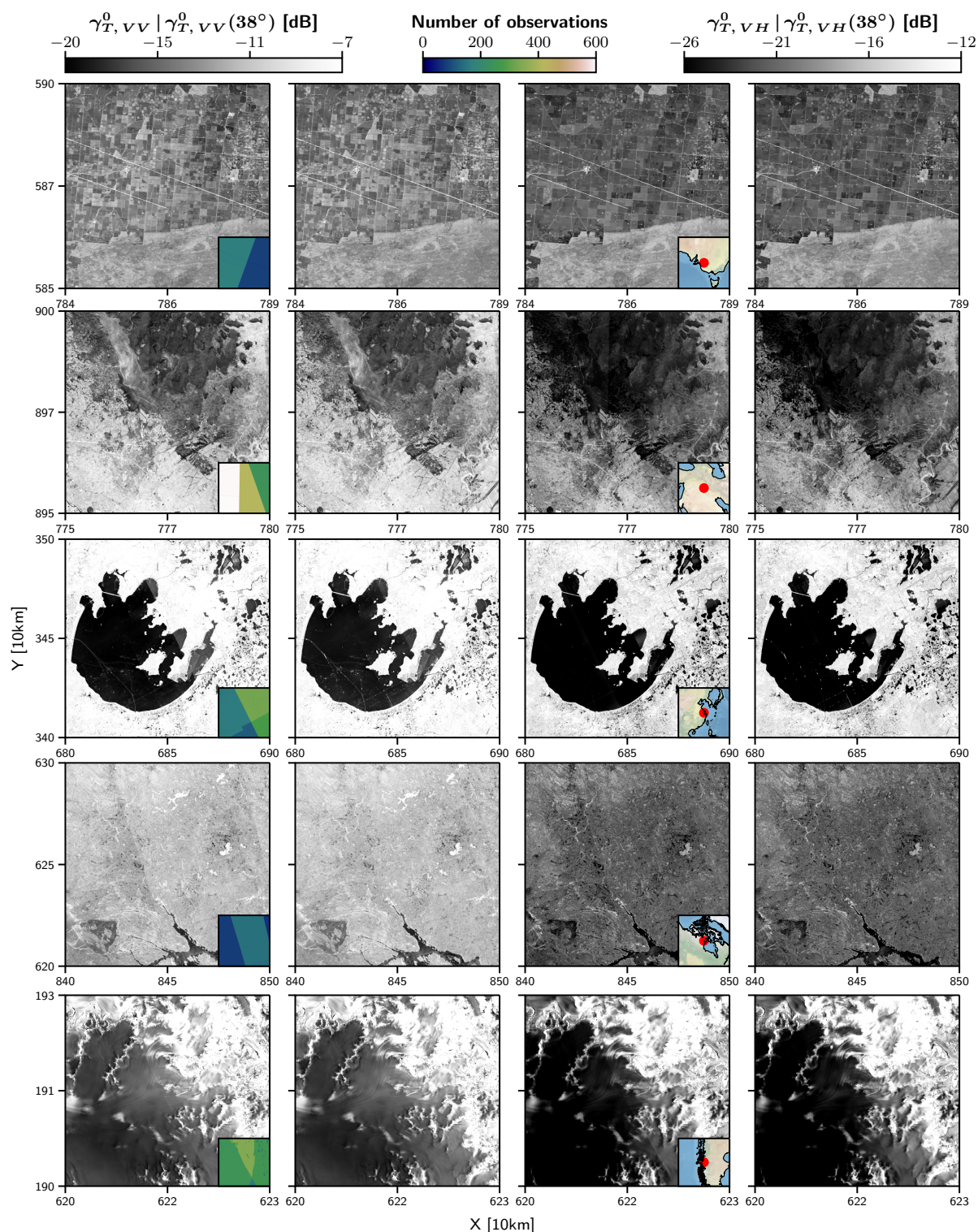


**Figure 11.** Radar backscatter composites generated from non-normalised backscatter ( $\gamma_T^0$ ; first and third columns) and normalised backscatter ( $\gamma_T^0(38^\circ)$ ; second and fourth columns). The radar backscatter composites in the first two columns were generated from VV polarised backscatter and the ones in the last two columns from VH polarised backscatter. The selected areas are located in southern Australia (first row), Iraq (second row), eastern China (third row), northern Canada (fourth row), and southern Chile (fifth row). The small boxes in the lower-right corner of the images in the first column show the number of observations. The red dots in the boxes in the lower-right corner of the images in the third column provide some geographical context and mark the centre of the region.

### 3.2.2. Twelve-Day Composites

Instead of creating composites by using the entire time series, short-term composites may enable dynamic, gap-filled land cover mapping. Small et al. [24] introduced twelve-day wide-area backscatter composites based on an LCA-weighted combination of  $\gamma_T^0$  from different orbits. Considering a period of 12 days is a good trade-off between the revisit frequency of the Sentinel-1 satellites and the impact of natural variability when extending the time window to aggregate measurements. Figure 12 presents a comparison between non-normalised ( $\gamma_T^0$ ); LCA-weighted, non-normalised ( $\gamma_{T,c}^0$ ); normalised ( $\gamma_T^0(38^\circ)$ ); and LCA-weighted, normalised  $\gamma_{T,c}^0(38^\circ)$  twelve-day radar backscatter composites combining all scenes within the period from 15 October 2020 to 27 October 2020. The VV polarised, normalised composites are entirely seamless and smooth, demonstrating the superior performance of normalisation using the estimated slope ( $\beta_e$ ). However, all VH polarised composites show an obvious orbital pattern, with a slightly weaker performance for the normalised ones. In addition to the effects of freezing and wind, an explanation could be that backscatter values observed at certain incidence angles are close to the noise floor of Sentinel-1's C-band sensor [30,65]. LCA-weighting seems to have no effect, since the strong forward scattering over water bodies prevails in terms of the difference in local resolution.

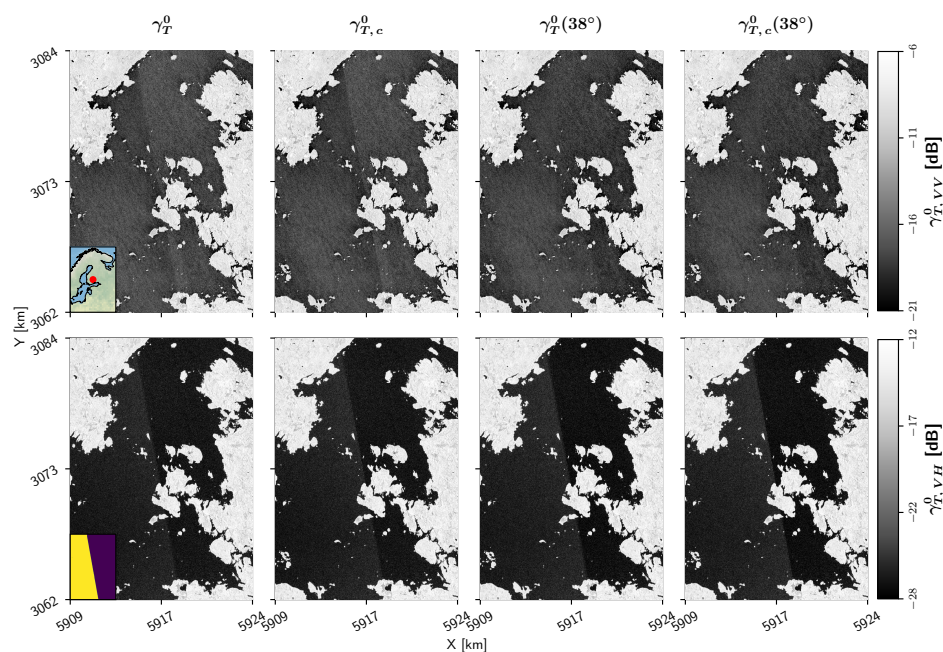


**Figure 12.** Comparison between a non-normalised ( $\gamma_T^0$ , first column); LCA-weighted, non-normalised ( $\gamma_{T,c}^0$ , second column); normalised ( $\gamma_T^0(38^\circ)$ , third column); and LCA-weighted, normalised ( $\gamma_{T,c}^0(38^\circ)$ , fourth column) twelve-day radar backscatter composites (15 October 2020–27 October 2020). The first row shows VV backscatter, and the second row shows VH backscatter. The small boxes in the lower-left corner of the first images in the first and second rows show the location of the selected area (Lake Näsijärvi, Finland) and the number of observations (yellow: 7; purple: 5), respectively.

## 4. Discussion

Some factors that make it difficult to obtain a reliable estimate of  $\beta$  have already been mentioned in the previous sections. The natural variability of backscatter in combination with a sparse angular coverage yields a high standard deviation of the calculated slopes ( $\sigma_\beta$ ), which directly affects the training and validation of the model (Section 3.1). Bio-geophysical processes, anthropogenic changes, and the impact of speckle alter the relationship between incidence angles and backscatter. Examples are frozen lakes in winter

(Figure 12), ship traffic (Lake Tai Hu in Figure 11), seasonal vegetation cycles and forest phenology [66], wind ripples, and snow melt. Uncertainties caused by daily variations of the land surface, e.g., day–night freezing (Section 2.3) and evapotranspiration, have already been mitigated by separating model training and prediction for each orbit direction. Another measure to counteract systematic temporal backscatter variations and to improve the overall performance of the FFNN would be to define the training and reference datasets and the sampling strategy for shorter time periods, e.g., seasons or months, instead of multiple years. Dynamic weight adjustments could then be used to evolve the model over time and improve the robustness with respect to sensor changes [67].

Additionally, we found a significant number of scenes affected by thermal noise, discontinuities at sub-swath boundaries, and Radiometric Frequency Interference (RFI) [68,69]. RFI could be observed near military bases and urban areas, e.g., in eastern China close to the metropolitan area of Suzhou (Figure 11), and impacts co- and cross-polarisations differently, polluting certain parameters more than others, thereby biasing the slope estimate. In addition, objects acting as corner reflectors show a polarisation dependence on the computed slope values (Figure 9, top). Another source of uncertainty might be changes in Sentinel-1's antenna pattern throughout the years [70]. Statistically, the VH model performs better, but this can be attributed to the lower incidence-angle dependency of VH backscatter. There are cases where one polarisation outperforms the other, e.g., as in Figure 12 or southern Australia in Figure 11, which is caused by temporal dynamics and the aforementioned noise contributions.

These uncertainties affect the input parameters differently than the calculated slope, leading to a disagreement between  $\beta_e$  and  $\beta_r$ , with an average RMSE value of 0.1 dB/° and an MAE of 0.05 dB/°. The introduced noise and the limited dynamic range of the input parameters might explain the observed underestimation of  $\beta_r$  by  $\beta_e$  of around 80% of the population. The initial approach to counteract the underestimation was to apply different sampling strategies for training, i.e., random sampling of balanced amounts of data across land cover types (A) and slope bins (B). The accuracy metrics for A and B turned out to be very similar, which shows that the sampling and model training are already robust. The estimation of extreme values is, in general, difficult for conventional machine learning methods. Since extreme-value data points occur only rarely, machine learning methods tend to learn mainly non-extreme data points [71]. But even under all these circumstances, the predictors still provide enough information to model  $\beta_e$ , with its mean value ( $\bar{\beta}_e$ ) being close to  $\bar{\beta}_r$  for most land cover types (Table 2).

Comparing land cover patterns in the input parameters with respect to the predicted slope (Figures 6 and 9) and the two-dimensional distributions in Figure 8 reveals that the most important variable is the sensitivity ( $\tilde{\gamma}_T^0$ ) of a specific polarisation, followed by CR sensitivity, with the average backscatter ( $\bar{\gamma}_T^0$ ) coming in last. The steepness of the slope is directly correlated with the spread of the backscatter distribution, which justifies the variable importance of  $\tilde{\gamma}_T^0$ .

Sentinel-1's acquisition strategy limits the number of available observations from different orbits, leading to the majority of Earth's land surface being only covered by one orbit (Figure 1, top). To overcome the under-determinacy of the linear system, other publications used an average slope estimate [27], a multi-variate regression solely based on backscatter [35], or no normalisation at all, instead using local-resolution weighted averaging for radar composites [24]. The advantage of our model is the higher complexity compared to that proposed in [35], allowing for consideration of more input parameters and operation at the spatial resolution of the SAR data, i.e., 20 m. In particular, the addition of the CR-based parameters proved beneficial to the model's performance. When dealing with RTC backscatter data, the impacts of static terrain and viewing geometry have already

been considered, making it more difficult to establish a reliable connection between statistical backscatter parameters and the slope ( $\beta$ ). Bauer-Marschallinger et al. [35] defined the relationship between  $\sigma^0$  and the incidence angle using three coefficients of a multivariate regression model, whereas our FFNN allows for a more complex mapping of input parameters to  $\beta$ . Even when our model is trained in regions being observed by two relative orbits per orbit direction, the information provided by the chosen input parameters also mitigates orbital artefacts in sparsely covered areas, e.g., in southern Australia and northern Canada in Figure 11. In regions where the SAR data are not contaminated with thermal noise or RFI, we observed a smooth transition across the orbital swath boundaries.

As seen in Figure 12, LCA-weighted averaging following the recipe of Small [72] has a very limited impact in terms of reducing orbital artefacts in composites containing objects with pronounced scattering characteristics. Compared to non-normalised backscatter data, LCA-weighted composites provide a significant advantage in undulated terrain, where local resolutions are strongly varying and infilling of shadow areas with data from other orbit directions comes in handy. After normalising the data, backscatter values are theoretically aligned to the local resolution at  $38^\circ$ . However, when combining data from different orbits or sensors, the actual detail and resolution of the observed signal still vary due to the difference in the illuminated area. LCA-weighted averaging is therefore key to providing a radiometrically meaningful estimate of the mean normalised backscatter.

However, we did not observe any major artefacts when simply averaging normalised backscatter from different orbit directions. This might be mainly due to the low number of orbital crossings, i.e., backscatter from ascending and descending directions, within our regions of interest for the selected time period. The only noticeable discrepancies arise due to the temporal variability in the slope estimates. The method of Small et al. [24,72] only considers static terrain information and is not affected by a temporal mismatch between the period of the estimated slope (three years in this case) and the time window of the aggregation (12 days to three years). Theoretically, since our model operates with the small set of parameters defined in Section 2.4, the current setup would even allow for the introduction of parameters covering the same time frame as the data used for compositing. This could provide significant improvements for short-term, normalised radar composites.

## 5. Conclusions

In this paper, we demonstrated the potential of a machine learning-based slope estimate that captures the linear behaviour between backscatter and incidence angles. The novelty of this approach is that it only requires information from backscatter time series and, thus, overcomes the constraints of the limited orbital coverage of the Sentinel-1 constellation. Sentinel-1's observation scheme and the narrow range of incidence angles add a high level of uncertainty to the reference slope values used to train with and validate against. Choosing statistical parameters representing the level and range of expected backscatter values and an FFNN allowed us to significantly reduce the noisy behaviour of the slope at the cost of a limited range of values. The final slope estimates contain valuable information on scattering characteristics of different land cover types and, thus, enable the modelling of strong forward scattering over water bodies and wetlands, moderate surface scattering over bare soil and sparsely vegetated areas, and volume scattering over forested areas.

Certain land cover types experience strong temporal variations, e.g., freeze–thaw cycles or snowfall over wetlands, water bodies, and alpine regions; forest phenology; and agricultural practices, which deteriorates the representativeness of a single slope value for the entire time series. This requires further research using a more granular land cover classification and a revised training and prediction approach for the FFNN. Instead of training the model on the entire time series, training samples could be selected from

temporal subsets such as seasonal or monthly intervals across several years. It would also be beneficial to not only train but also estimate slope values for shorter time periods, resulting in a better match of land cover conditions. Since the FFNN only requires a few static input layers, which can be derived by aggregating backscatter data over any time period, the whole setup is highly flexible and scaleable. Moreover, the FFNN bypasses the computational burden of fitting a physically based model to backscatter-incidence angle measurements, enabling the trained model to be applied efficiently on a global scale.

After using the slope to normalise backscatter data to a certain reference angle, i.e.,  $38^\circ$ , it is possible to generate seamless normalised radar backscatter composites. Other methods producing analysis-ready backscatter composites [24] use static terrain-based information to aggregate data but do not consider any physical aspects, such as scattering characteristics. Thus, orbital patterns remain for land cover types with a pronounced backscatter–incidence angle dependency. The novel composites presented in this paper are able to mitigate these orbital artefacts, marking an important step forward in offering analysis-ready backscatter data. They will be valuable to the EO user community in the realms of land cover and land use mapping [24], as well as for the radiometric calibration of sensors [27]. As we look forward to the launches of Sentinel-1 C/D and NISAR at the beginning of 2025, the golden era of SAR will continue to offer a valuable data stream to improve our presented machine learning model and to generate seamless analysis-ready radar backscatter composites.

**Author Contributions:** Conceptualisation, C.N., F.R. and W.W.; methodology, C.N., F.R. and W.W.; software, C.N. and F.R.; validation, C.N.; formal analysis, C.N.; investigation, C.N.; resources, C.N.; data curation, C.N.; writing—original draft preparation, C.N.; writing—review and editing, C.N., F.R., and W.W.; visualisation, C.N.; supervision, W.W. All authors have read and agreed to the published version of the manuscript.

**Funding:** This research received no external funding.

**Data Availability Statement:** The original contributions presented in the study are included in the article, further inquiries can be directed to the corresponding author.

**Acknowledgments:** The authors would like to thank Bernhard Bauer-Marschallinger and Bernhard Raml for initial discussions on conceptualising the work and Thomas Melzer for his advice on error characterisation. The presented computational results were achieved, in part, using the VSC and the cloud computing environment of EODC. In addition, we want to express our gratitude to the reviewers for their highly valuable comments and acknowledge TU Wien Bibliothek for financial support through its Open Access Funding Programme.

**Conflicts of Interest:** The authors declare no conflicts of interest.

## Abbreviations

The following abbreviations are used in this manuscript:

ARD	Analysis-Ready Data
AVE	Angular Variation Effect
CEOS	Committee on Earth Observation Satellites
CR	Cross-Ratio
DEM	Digital Elevation Model
EO	Earth Observation
EODC	Earth Observation Data Centre for water resources monitoring
ESA	European Space Agency
FFNN	Feed-Forward Neural Network
GRD	Ground Range Detected
GTC	Geometric Terrain Correction
IDR	Inter-Decile Range

IPF	Instrument Processing Facility
IW	Interferometric Wide swath mode
LCA	Local Contributing Area
MAE	Mean Average Error
ML	Machine Learning
NN	Neural Network
NRB	Normalised Radar Backscatter
POA	Polarimetric Orientation Angle
RCM	RADARSAT Constellation Mission
RMSE	Root Mean Squared Error
RTC	Radiometric Terrain Correction
SAR	Synthetic Aperture Radar
VSC	Vienna Scientific Cluster

## References

1. Wagner, W. *Soil Moisture Retrieval from ERS Scatterometer Data*; Inst. für Photogrammetrie u. Fernerkundung d. Techn. Univ.: Vienna, Austria, 1998.
2. De Zan, F.; Parizzi, A.; Prats-Iraola, P.; López-Dekker, P. A SAR interferometric model for soil moisture. *IEEE Trans. Geosci. Remote Sens.* **2013**, *52*, 418–425. [[CrossRef](#)]
3. Kellndorfer, J.M.; Pierce, L.E.; Dobson, M.C.; Ulaby, F.T. Toward consistent regional-to-global-scale vegetation characterization using orbital SAR systems. *IEEE Trans. Geosci. Remote Sens.* **1998**, *36*, 1396–1411. [[CrossRef](#)]
4. Dostálová, A.; Lang, M.; Ivanovs, J.; Waser, L.T.; Wagner, W. European wide forest classification based on sentinel-1 data. *Remote Sens.* **2021**, *13*, 337. [[CrossRef](#)]
5. Nagler, T.; Rott, H.; Ripper, E.; Bippus, G.; Hetzenecker, M. Advancements for snowmelt monitoring by means of sentinel-1 SAR. *Remote Sens.* **2016**, *8*, 348. [[CrossRef](#)]
6. Shi, J.; Dozier, J.; Rott, H. Snow mapping in alpine regions with synthetic aperture radar. *IEEE Trans. Geosci. Remote Sens.* **1994**, *32*, 152–158.
7. Twele, A.; Cao, W.; Plank, S.; Martinis, S. Sentinel-1-based flood mapping: A fully automated processing chain. *Int. J. Remote Sens.* **2016**, *37*, 2990–3004. [[CrossRef](#)]
8. Bauer-Marschallinger, B.; Cao, S.; Tupas, M.E.; Roth, F.; Navacchi, C.; Melzer, T.; Freeman, V.; Wagner, W. Satellite-Based Flood Mapping through Bayesian Inference from a Sentinel-1 SAR Datacube. *Remote Sens.* **2022**, *14*, 3673. [[CrossRef](#)]
9. Clapp, R.E. *A Theoretical and Experimental Study of Radar Ground Return*; Radiation Laboratory, Massachusetts Institute of Technology: Cambridge, MA, USA, 1946.
10. Cosgriff, R.; Peake, W.; Taylor, R. *Terrain Scattering Properties for Sensor System Design (Terrain Handbook No. II)*; Columbus Antenna Laboratory, College of Engineering, Ohio State University: Columbus, OH, USA, 1960.
11. Ulaby, F.T.; Moore, R.K.; Fung, A.K. *Microwave Remote Sensing: Active and Passive. Volume 2-Radar Remote Sensing and Surface Scattering and Emission Theory*; Addison-Wesley: Reading, MA, USA, 1982.
12. Hoekman, D.H.; Reiche, J. Multi-model radiometric slope correction of SAR images of complex terrain using a two-stage semi-empirical approach. *Remote Sens. Environ.* **2015**, *156*, 1–10. [[CrossRef](#)]
13. Ulander, L.M. Radiometric slope correction of synthetic-aperture radar images. *IEEE Trans. Geosci. Remote Sens.* **1996**, *34*, 1115–1122. [[CrossRef](#)]
14. Loew, A.; Mauser, W. Generation of geometrically and radiometrically terrain corrected SAR image products. *Remote Sens. Environ.* **2007**, *106*, 337–349. [[CrossRef](#)]
15. Vollrath, A.; Mullissa, A.; Reiche, J. Angular-based radiometric slope correction for Sentinel-1 on google earth engine. *Remote Sens.* **2020**, *12*, 1867. [[CrossRef](#)]
16. Small, D.; Holecz, F.; Meier, E.; Nuesch, D. Absolute radiometric correction in rugged terrain: A plea for integrated radar brightness. In Proceedings of the IGARSS '98. Sensing and Managing the Environment. 1998 IEEE International Geoscience and Remote Sensing. Symposium Proceedings. (Cat. No.98CH36174), Seattle, WA, USA, 6–10 July 1998; Volume 1, pp. 330–332.
17. Small, D. Flattening gamma: Radiometric terrain correction for SAR imagery. *IEEE Trans. Geosci. Remote Sens.* **2011**, *49*, 3081–3093. [[CrossRef](#)]
18. Charbonneau, F.; Rosenqvist, A.; Truckenbrodt, J.; Albinet, C.; Small, D.; Chapman, B.; Zebker, H.; Dadamia, D.; Deschamps, B.; Hajduch, G.; et al. Combined CEOS-ARD for Synthetic Aperture Radar. CEOS, 2023. Version 1.0. Available online: [https://ceos.org/ard/files/PFS/SAR/v1.0/CEOS-ARD\\_PFS\\_Synthetic\\_Aperture\\_Radar\\_v1.0.pdf](https://ceos.org/ard/files/PFS/SAR/v1.0/CEOS-ARD_PFS_Synthetic_Aperture_Radar_v1.0.pdf) (accessed on 1 August 2024).

19. Flores-Anderson, A.I.; Parache, H.B.; Martin-Arias, V.; Jiménez, S.A.; Herndon, K.; Mehlich, S.; Meyer, F.J.; Agarwal, S.; Ilyushchenko, S.; Agarwal, M.; et al. Evaluating SAR Radiometric Terrain Correction Products: Analysis-Ready Data for Users. *Remote Sens.* **2023**, *15*, 5110. [CrossRef]
20. Dostalova, A.; Navacchi, C.; Greimeister-Pfeil, I.; Small, D.; Wagner, W. The effects of radiometric terrain flattening on SAR-based forest mapping and classification. *Remote Sens. Lett.* **2022**, *13*, 855–864. [CrossRef]
21. Rüetschi, M.; Schaepman, M.E.; Small, D. Using multitemporal sentinel-1 c-band backscatter to monitor phenology and classify deciduous and coniferous forests in northern switzerland. *Remote Sens.* **2017**, *10*, 55. [CrossRef]
22. Small, D.; Miranda, N.; Ewen, T.; Jonas, T. Reliably flattened radar backscatter for wet snow mapping from wide-swath sensors. In Proceedings of the ESA Living Planet Symposium, Edinburgh, Scotland, 9–13 September 2013.
23. Navacchi, C.; Cao, S.; Bauer-Marschallinger, B.; Snoeij, P.; Small, D.; Wagner, W. Utilising Sentinel-1's Orbital Stability for Efficient Pre-Processing of Radiometric Terrain Corrected Gamma Nought Backscatter. *Sensors* **2023**, *23*, 6072. [CrossRef]
24. Small, D.; Rohner, C.; Miranda, N.; Rüetschi, M.; Schaepman, M.E. Wide-area analysis-ready radar backscatter composites. *IEEE Trans. Geosci. Remote Sens.* **2021**, *60*, 5201814. [CrossRef]
25. Hahn, S.; Reimer, C.; Vreugdenhil, M.; Melzer, T.; Wagner, W. Dynamic characterization of the incidence angle dependence of backscatter using Metop ASCAT. *IEEE J. Sel. Top. Appl. Earth Obs. Remote Sens.* **2017**, *10*, 2348–2359. [CrossRef]
26. O'Grady, D.; Leblanc, M.; Bass, A. The use of radar satellite data from multiple incidence angles improves surface water mapping. *Remote Sens. Environ.* **2014**, *140*, 652–664. [CrossRef]
27. Bauer-Marschallinger, B.; Cao, S.; Navacchi, C.; Freeman, V.; Reuß, F.; Geudtner, D.; Rommen, B.; Vega, F.C.; Snoeij, P.; Attema, E.; et al. The normalised Sentinel-1 Global Backscatter Model, mapping Earth's land surface with C-band microwaves. *Sci. Data* **2021**, *8*, 277. [CrossRef]
28. O'Grady, D.; Leblanc, M.; Gillieson, D. Relationship of local incidence angle with satellite radar backscatter for different surface conditions. *Int. J. Appl. Earth Obs. Geoinf.* **2013**, *24*, 42–53. [CrossRef]
29. Castel, T.; Beaudoin, A.; Stach, N.; Stussi, N.; Le Toan, T.; Durand, P. Sensitivity of space-borne SAR data to forest parameters over sloping terrain. Theory and experiment. *Int. J. Remote Sens.* **2001**, *22*, 2351–2376. [CrossRef]
30. Aldenhoff, W.; Eriksson, L.E.; Ye, Y.; Heuzé, C. First-year and multiyear sea ice incidence angle normalization of dual-polarized Sentinel-1 SAR images in the Beaufort Sea. *IEEE J. Sel. Top. Appl. Earth Obs. Remote Sens.* **2020**, *13*, 1540–1550. [CrossRef]
31. Zhao, L.; Chen, E.; Li, Z.; Zhang, W.; Gu, X. Three-step semi-empirical radiometric terrain correction approach for PolSAR data applied to forested areas. *Remote Sens.* **2017**, *9*, 269. [CrossRef]
32. Villard, L.; Le Toan, T. Relating P-Band SAR Intensity to Biomass for Tropical Dense Forests in Hilly Terrain:  $\gamma^0$  or  $t^0$ ? *IEEE J. Sel. Top. Appl. Earth Obs. Remote Sens.* **2014**, *8*, 214–223. [CrossRef]
33. Chen, X.; Li, G.; Chen, Z.; Ju, Q.; Cheng, X. Incidence angle normalization of dual-polarized Sentinel-1 backscatter data on Greenland Ice Sheet. *Remote Sens.* **2022**, *14*, 5534. [CrossRef]
34. Quast, R.; Wagner, W.; Bauer-Marschallinger, B.; Vreugdenhil, M. Soil moisture retrieval from Sentinel-1 using a first-order radiative transfer model—A case-study over the Po-Valley. *Remote Sens. Environ.* **2023**, *295*, 113651. [CrossRef]
35. Bauer-Marschallinger, B.; Freeman, V.; Cao, S.; Paulik, C.; Schaufler, S.; Stachl, T.; Modanesi, S.; Massari, C.; Ciabatta, L.; Brocca, L.; et al. Toward global soil moisture monitoring with Sentinel-1: Harnessing assets and overcoming obstacles. *IEEE Trans. Geosci. Remote Sens.* **2018**, *57*, 520–539. [CrossRef]
36. Paluba, D.; Laštovička, J.; Mouratidis, A.; Štych, P. Land cover-specific local incidence angle correction: A method for time-series analysis of forest ecosystems. *Remote Sens.* **2021**, *13*, 1743. [CrossRef]
37. Torres, R.; Snoeij, P.; Geudtner, D.; Bibby, D.; Davidson, M.; Attema, E.; Potin, P.; Rommen, B.; Floury, N.; Brown, M.; et al. GMES Sentinel-1 mission. *Remote Sens. Environ.* **2012**, *120*, 9–24. [CrossRef]
38. Potin, P.; Rosich, B.; Grimont, P.; Miranda, N.; Shurmer, I.; O'Connell, A.; Torres, R.; Krassenburg, M. Sentinel-1 mission status. In Proceedings of the EUSAR 2016: 11th European Conference on Synthetic Aperture Radar, Hamburg, Germany, 6–9 June 2016; pp. 1–6.
39. Wagner, W.; Lemoine, G.; Borgeaud, M.; Rott, H. A study of vegetation cover effects on ERS scatterometer data. *IEEE Trans. Geosci. Remote Sens.* **1999**, *37*, 938–948. [CrossRef]
40. ESA. ESA WorldCover 2021. 2021. Available online: <https://worldcover2021.esa.int/> (accessed on 2 June 2024).
41. Wagner, W.; Bauer-Marschallinger, B.; Navacchi, C.; Reuß, F.; Cao, S.; Reimer, C.; Schramm, M.; Briese, C. A Sentinel-1 backscatter datacube for global land monitoring applications. *Remote Sens.* **2021**, *13*, 4622. [CrossRef]
42. Fahrland, E. Copernicus Digital Elevation Model Product Handbook. Airbus, Version 5.0. 2022. Available online: [https://dataspace.copernicus.eu/sites/default/files/media/files/2024-06/geo1988-copernicusdem-spe-002\\_producthandbook\\_i5.0.pdf](https://dataspace.copernicus.eu/sites/default/files/media/files/2024-06/geo1988-copernicusdem-spe-002_producthandbook_i5.0.pdf) (accessed on 15 January 2025).
43. Bauer-Marschallinger, B.; Sabel, D.; Wagner, W. Optimisation of global grids for high-resolution remote sensing data. *Comput. Geosci.* **2014**, *72*, 84–93. [CrossRef]

44. EODC. Earth Observation Data Centre. 2024. Available online: <https://eodc.eu/> (accessed on 1 August 2024).
45. VSC. VSC-5—Newest System Featuring CPU and GPU. 2024. Available online: <https://vsc.ac.at//systems/vsc-5/> (accessed on 1 August 2024).
46. Miranda, N.; Hajduch, G. S-1 Mission Performance Centre Masking “No-value” Pixels on GRD Products Generated by the Sentinel-1 ESA IPF. ESA, 2018. Issue 2.1. Available online: <https://sentinel.esa.int/documents/247904/2142675/Sentinel-1-masking-no-value-pixels-grd-products-note> (accessed on 1 August 2024).
47. Ali, I.; Cao, S.; Naeimi, V.; Paulik, C.; Wagner, W. Methods to remove the border noise from Sentinel-1 synthetic aperture radar data: Implications and importance for time-series analysis. *IEEE J. Sel. Top. Appl. Earth Obs. Remote Sens.* **2018**, *11*, 777–786. [[CrossRef](#)]
48. ESA. Sentinel-1 New Product Format Operational on 13 March 2018. Available online: <https://scihub.copernicus.eu/news/News00301> (accessed on 7 June 2024).
49. ESA. Mission Ends for Copernicus Sentinel-1B Satellite. 2022. Available online: [https://www.esa.int/Applications/Observing\\_the\\_Earth/Copernicus/Sentinel-1/Mission\\_ends\\_for\\_Copernicus\\_Sentinel-1B\\_satellite](https://www.esa.int/Applications/Observing_the_Earth/Copernicus/Sentinel-1/Mission_ends_for_Copernicus_Sentinel-1B_satellite) (accessed on 1 August 2024).
50. Navacchi, C.; Cao, S.; Bauer-Marschallinger, B.; Snoeij, P.; Small, D.; Wagner, W. Utilising Sentinel-1’s orbital stability for efficient pre-processing of sigma nought backscatter. *ISPRS J. Photogramm. Remote Sens.* **2022**, *192*, 130–141. [[CrossRef](#)]
51. ESA. POD Products and Requirements. 2023. Available online: <https://sentinel.esa.int/web/sentinel/technical-guides/sentinel-1-sar/pod/products-requirements> (accessed on 30 January 2023).
52. Agram, P.S.; Warren, M.S.; Arko, S.A.; Calef, M.T. Radiometric Terrain Flattening of Geocoded Stacks of SAR Imagery. *Remote Sens.* **2023**, *15*, 1932. [[CrossRef](#)]
53. Ulaby, F.T.; Moore, R.K.; Fung, A.K. *Microwave Remote Sensing: Active and Passive. Volume 1-Microwave Remote Sensing Fundamentals and Radiometry*; Artech House: Washington, DC, USA, 1981.
54. Naeimi, V.; Bartalis, Z.; Wagner, W. ASCAT soil moisture: An assessment of the data quality and consistency with the ERS scatterometer heritage. *J. Hydrometeorol.* **2009**, *10*, 555–563. [[CrossRef](#)]
55. Howell, D.C. *Statistical Methods for Psychology*, 7th ed.; Cengage Wadsworth: Belmont, CA, USA, 2010.
56. Schaufler, S.; Bauer-Marschallinger, B.; Hochstöger, S.; Wagner, W. Modelling and correcting azimuthal anisotropy in Sentinel-1 backscatter data. *Remote Sens. Lett.* **2018**, *9*, 799–808. [[CrossRef](#)]
57. Bowen, B.B.; Kipnis, E.L.; Raming, L.W. Temporal dynamics of flooding, evaporation, and desiccation cycles and observations of salt crust area change at the Bonneville Salt Flats, Utah. *Geomorphology* **2017**, *299*, 1–11. [[CrossRef](#)]
58. Raney, R.K. Radar fundamentals: Technical perspective. *Princ. Appl. Imaging Radar Man. Remote Sens.* **1998**, *2*, 9–130.
59. Woodhouse, I.H. *Introduction to Microwave Remote Sensing*; Taylor & Francis: Abingdon, UK, 2006.
60. Dong, Y.; Forster, B.; Ticehurst, C. Radar backscatter analysis for urban environments. *Int. J. Remote Sens.* **1997**, *18*, 1351–1364. [[CrossRef](#)]
61. Vreugdenhil, M.; Navacchi, C.; Bauer-Marschallinger, B.; Hahn, S.; Steele-Dunne, S.; Pfeil, I.; Dorigo, W.; Wagner, W. Sentinel-1 cross ratio and vegetation optical depth: A comparison over Europe. *Remote Sens.* **2020**, *12*, 3404. [[CrossRef](#)]
62. McCulloch, W.S.; Pitts, W. A logical calculus of the ideas immanent in nervous activity. *Bull. Math. Biophys.* **1943**, *5*, 115–133. [[CrossRef](#)]
63. Liebe, J.R.; van de Giesen, N.; Andreini, M.S.; Steenhuis, T.S.; Walter, M.T. Suitability and limitations of ENVISAT ASAR for monitoring small reservoirs in a semiarid area. *IEEE Trans. Geosci. Remote Sens.* **2008**, *47*, 1536–1547. [[CrossRef](#)]
64. Bauer-Marschallinger, B. The Equi7Grid V14: Grid and Tiling Definition Document. TU Wien, 2023. Issue 0.8. Available online: [https://github.com/TUW-GEO/Equi7Grid/blob/master/docs/doc\\_files/EQUI7\\_V14\\_grid\\_and\\_tiling\\_definition\\_document\\_issue08.pdf](https://github.com/TUW-GEO/Equi7Grid/blob/master/docs/doc_files/EQUI7_V14_grid_and_tiling_definition_document_issue08.pdf) (accessed on 1 August 2024).
65. Schmidt, K.; Schwerdt, M.; Miranda, N.; Reimann, J. Radiometric comparison within the Sentinel-1 SAR constellation over a wide backscatter range. *Remote Sens.* **2020**, *12*, 854. [[CrossRef](#)]
66. Borlaf-Mena, I.; García-Duro, J.; Santoro, M.; Villard, L.; Badea, O.; Tanase, M.A. Seasonality and directionality effects on radar backscatter are key to identify mountain forest types with Sentinel-1 data. *Remote Sens. Environ.* **2023**, *296*, 113728. [[CrossRef](#)]
67. Rakitianskaia, A.; Engelbrecht, A.P. Training neural networks with PSO in dynamic environments. In Proceedings of the 2009 IEEE Congress on Evolutionary Computation, Trondheim, Norway, 18–21 May 2009; pp. 667–673.
68. Park, J.W.; Korosov, A.A.; Babiker, M.; Sandven, S.; Won, J.S. Efficient thermal noise removal for Sentinel-1 TOPSAR cross-polarization channel. *IEEE Trans. Geosci. Remote Sens.* **2017**, *56*, 1555–1565. [[CrossRef](#)]
69. Leng, X.; Ji, K.; Kuang, G. Radio frequency interference detection and localization in Sentinel-1 images. *IEEE Trans. Geosci. Remote Sens.* **2021**, *59*, 9270–9281. [[CrossRef](#)]
70. Schmidt, K.; Schwerdt, M.; Hajduch, G.; Vincent, P.; Recchia, A.; Pinheiro, M. Radiometric Re-Compensation of Sentinel-1 SAR Data Products for Artificial Biases due to Antenna Pattern Changes. *Remote Sens.* **2023**, *15*, 1377. [[CrossRef](#)]

71. Ding, D.; Zhang, M.; Pan, X.; Yang, M.; He, X. Modeling extreme events in time series prediction. In Proceedings of the 25th ACM SIGKDD International Conference on Knowledge Discovery & Data Mining, Anchorage, AK, USA, 4–8 August 2019; pp. 1114–1122.
72. Small, D. SAR backscatter multitemporal compositing via local resolution weighting. In Proceedings of the 2012 IEEE International Geoscience and Remote Sensing Symposium, Munich, Germany, 22–27 July 2012; pp. 4521–4524.

**Disclaimer/Publisher’s Note:** The statements, opinions and data contained in all publications are solely those of the individual author(s) and contributor(s) and not of MDPI and/or the editor(s). MDPI and/or the editor(s) disclaim responsibility for any injury to people or property resulting from any ideas, methods, instructions or products referred to in the content.